



**HAL**  
open science

# Ambient-noise tomography of the Ligurian-Provence Basin using the AlpArray onshore-offshore network: Insights for the oceanic domain structure

Ahmed Nouibat, Laurent Stehly, Anne Paul, Stéphane Schwartz, Yann Rolland, Thierry Dumont, W C Crawford, Romain Brossier

## ► To cite this version:

Ahmed Nouibat, Laurent Stehly, Anne Paul, Stéphane Schwartz, Yann Rolland, et al.. Ambient-noise tomography of the Ligurian-Provence Basin using the AlpArray onshore-offshore network: Insights for the oceanic domain structure. *Journal of Geophysical Research: Solid Earth*, 2022, 127, pp.e2022JB024228. 10.1029/2022jb024228 . hal-03719400

**HAL Id: hal-03719400**

**<https://hal.science/hal-03719400v1>**

Submitted on 11 Jul 2022

**HAL** is a multi-disciplinary open access archive for the deposit and dissemination of scientific research documents, whether they are published or not. The documents may come from teaching and research institutions in France or abroad, or from public or private research centers.

L'archive ouverte pluridisciplinaire **HAL**, est destinée au dépôt et à la diffusion de documents scientifiques de niveau recherche, publiés ou non, émanant des établissements d'enseignement et de recherche français ou étrangers, des laboratoires publics ou privés.

# Ambient-noise tomography of the Ligurian-Provence Basin using the AlpArray onshore-offshore network: Insights for the oceanic domain structure

A. Nouibat<sup>1</sup>, L. Stehly<sup>1</sup>, A. Paul<sup>1</sup>, S. Schwartz<sup>1</sup>, Y. Rolland<sup>1,2</sup>, T. Dumont<sup>1</sup>,  
W. C. Crawford<sup>3</sup>, R. Brossier<sup>1</sup>, Cifalps Team, and AlpArray Working Group\*

<sup>1</sup>Univ. Grenoble Alpes, Univ. Savoie Mont Blanc, CNRS, IRD, UGE, ISTerre, 38000 Grenoble, France

<sup>2</sup>Univ. Savoie Mont Blanc, CNRS, UMR 5204, EDYTEM, 73370 Le Bourget-du-Lac, France

<sup>3</sup>Institut de Physique du Globe de Paris, Sorbonne Paris Cité, 75005 Paris, France

## Key Points:

- Efficient processing scheme to remove transients and reduce tilt and compliance from continuous ambient noise recorded by OBSs
- Computation of iterative correlations between OBSs based on a virtual reconstruction of the Rayleigh waves
- Thin, anomalous oceanic crust with gabbroic intrusions evidenced in the basin axis from a joint interpretation of  $V_s$  and  $V_p$  models

\*AlpArray Working Group, <http://www.alparray.ethz.ch/home/>

Corresponding author: A. Nouibat, [ahmed.nouibat@univ-grenoble-alpes.fr](mailto:ahmed.nouibat@univ-grenoble-alpes.fr)

This article has been accepted for publication and undergone full peer review but has not been through the copyediting, typesetting, pagination and proofreading process, which may lead to differences between this version and the [Version of Record](#). Please cite this article as doi: [10.1029/2022JB024228](https://doi.org/10.1029/2022JB024228).

This article is protected by copyright. All rights reserved.

**Abstract**

We derive a three-dimensional shear-wave velocity model of the Ligurian-Provence back-arc basin (Northwestern Mediterranean Sea) using ocean-bottom seismometers (AlpArray OBSs) and land stations from permanent and temporary seismic networks. The quality of OBS continuous records is enhanced by a specific processing that reduces instrumental and seabed-induced noises (transients, tilt, compliance). To further improve the resolution of ambient-noise tomography in the offshore area, we compute the Rayleigh-wave part of the Green functions for OBS-OBS pairs by using onshore stations as virtual sources. 2-D group-velocity maps and their uncertainties are computed in the 4 - 150 s period range by a transdimensional inversion of Rayleigh-wave travel times. The dispersion data and their uncertainties are inverted for a probabilistic 3-D shear-wave velocity model that includes probability densities for  $V_s$  and for the depth of layer interfaces. The probabilistic model is refined by a linearized inversion that accounts for the water layer in the Ligurian Sea. Our  $S$ -wave velocity and layer boundary probability models correspond well to a recent, high-resolution  $P$ -wave velocity cross-section derived from controlled-source seismic profiling along the Ligurian-Provence basin axis. A joint interpretation of the  $P$ - and  $S$ -wave velocity sections along this profile reveals a thin, anomalous oceanic crust of low  $P$ -wave velocities but high  $S$ -wave velocities, intruded by a gabbroic body. The illuminated part of the upper mantle appears to be devoid of serpentinization.

**Plain Language Summary**

The Ligurian-Provence basin (Northwestern Mediterranean Sea) is one of the Miocene-Pliocene back-arc basins that resulted from the retreat of the Adria subduction in the plate reorganization due to Africa-Europe convergence. The crustal structure of the basin is still debated, even though it has been probed by active seismic profiling. We compute a high-resolution shear-wave velocity model of the Ligurian-Provence basin and its margins by making optimal use of ambient-noise recordings of seafloor broadband seismometers. In particular, we improve the usually low quality of surface-wave signals in noise correlations between seafloor stations by involving correlations with land stations. The joint interpretation of our  $S$ -wave velocity model with a  $P$ -wave velocity section obtained in the basin axis by controlled-source seismic profiling provides compelling evidence for the presence of a thick sediment pile above a thin,  $\sim 4.5$  km-thick oceanic crust, intruded by gabbroic bodies emplaced at the crust-mantle transition. These results show the potential of a joint

48 interpretation of  $P$ - and  $S$ -wave velocity models since they provide reliable answers to a  
49 number of debated questions on the petrological nature of the crust and uppermost mantle,  
50 in particular in the Ligurian-Provence basin.

## 51 **1 Introduction**

52 In the last two decades, the deployment of extensive and dense seismic networks of tem-  
53 porary broadband sensors (e.g., USArray, IberArray) has provided a better understanding  
54 of the deep structures of the crust and upper mantle, in particular through the emergence  
55 of increasingly more precise 3-D seismic imaging (e.g., Moschetti et al., 2010; Levander et  
56 al., 2011). However, many of these dense arrays included exclusively onshore sensors, thus  
57 preventing 3-D imaging of continent-ocean transitions and oceanic domains. The AlpArray  
58 seismic network (AASN) that covers the European Alps and their foreland, is one of the few  
59 dense seismic networks consisting of both onshore and offshore stations (Fig. 1; Hetényi et al.,  
60 2018). The onshore AASN has been used in ambient-noise imaging studies at the scale of the  
61 Alps and Apennines to construct 3-D models of shear-wave velocity (Lu et al., 2018, 2020),  
62 attenuation (coda-Q, Soergel et al., 2020), and radial anisotropy (Alder et al., 2021), as well  
63 as at the regional scale, e.g., Vienna basin (Schippkus et al., 2018), Western Alps (Zhao  
64 et al., 2020), Southeastern Alps (Sadeghi-Bagherabadi et al., 2021) and Bohemian Massif  
65 (Kvapil et al., 2021). The German-French ocean-bottom seismometers (OBS) of the AlpAr-  
66 ray network have been deployed to gain insights into the 3-D structure of the lithosphere  
67 beneath the Ligurian-Provence basin and its margins, where major geological/geodynamical  
68 issues remain to be clarified. The OBS recordings have been used together with data of on-  
69 shore permanent and temporary stations in the transdimensional ambient-noise tomography  
70 of Nouibat et al. (2022) that covers a large part of Western Europe. In Nouibat et al. (2022),  
71 we described the probabilistic inversion strategy for Rayleigh-wave group-velocity maps and  
72 their uncertainties, the injection of these uncertainties in the inversion for the  $V_s$  model,  
73 and the validity of the model in the southwestern Alps. The present paper is a complement  
74 to Nouibat et al. (2022) that focuses on the Ligurian-Provence basin. We describe here  
75 the specific processing of OBS records and the use of iterative noise correlations that are  
76 required to improve ray coverage in the Ligurian Sea, hence improving the model resolution  
77 in the basin. We further explain how the water layer and its thickness changes are taken  
78 into account in the inversion for  $S$ -wave velocity. Finally, we compare our  $V_s$  model to a  $V_p$   
79 section derived from controlled-source seismic profiling along the basin axis.

80 The geodynamic context of the western Mediterranean region is controlled by the  
81 northward motion of Africa (1 cm/yr) with respect to Europe since Late Cretaceous times  
82 (Fig. 1). This global convergence was accommodated by several collision episodes involving  
83 Europe with continental micro-plates (Iberia and Adria), leading to the formation of peri-  
84 mediterranean mountain belts (Alps, Apennines, Pyrenees, Dinarides and Betics; e.g., van  
85 Hinsbergen et al., 2020). During Miocene and Pliocene times, part of this convergence was  
86 accommodated by development of back-arc extensional basins behind the Adria northwest-  
87 dipping subduction zone (e.g., Gueguen et al., 1998; Jolivet et al., 2020). This extension  
88 started in the Ligurian-Provence basin, and has further spread from west to east, resulting  
89 in the opening of the Algerian basin, and later, of the Tyrrhenian basin (e.g., Séranne,  
90 1999; Rollet et al., 2002). Crustal thinning in the central Ligurian basin resulted in the  
91 formation of a narrow oceanic domain mainly identified from geophysical data, including  
92 seismic reflection, refraction and wide-angle profiling (e.g., Egger et al., 1988; Déverchère &  
93 Beslier, 1995; Dannowski et al., 2020), altimetry data and magnetic data from aeromagnetic  
94 surveys and reduction to the pole (Sandwell et al., 1995). Although the crust of the central  
95 Ligurian basin is considered "atypical" because it is thinner than normal oceanic crust and  
96 highlights non-linear magnetic anomalies and a concomitant low gravity anomaly (Bayer  
97 et al., 1973; Sandwell & Smith, 1997; Rollet et al., 2002), its petrological and lithological  
98 nature is poorly constrained and still debated. Several hypotheses have been considered: (1)  
99 thin oceanic crust with tholeiitic volcanism overlying mantle rocks, similar to the Tyrrhenian  
100 sea (e.g., Mascle & Rehault, 1990; Bonatti et al., 1990); (2) partly serpentinized peridotites  
101 of exhumed upper mantle mostly devoid of volcanic crust (e.g., Boillot et al., 1989; Beslier  
102 et al., 1993; Jolivet et al., 2020); (3) thinned and stretched continental crust related to an  
103 hyper-extended margin (e.g., McKenzie, 1978; Pascal et al., 1993; Dannowski et al., 2020).

104 We combine the OBS records of the AlpArray network with those of 890 onshore stations  
105 from the AlpArray temporary network, the Cifalps-2 temporary experiment and European  
106 permanent networks (Fig. 1). Ambient-noise data recorded by OBSs have already been  
107 used to build shear-wave velocity and anisotropy models in different regions, e.g., South-  
108 central Pacific (Harmon et al., 2007), Southeast of Tahiti Island (Takeo et al., 2016) and  
109 Western Indian Ocean (Hable et al., 2019). The originality of our approach lies in the  
110 specific processing of OBS records and their use within an innovative tomographic framework  
111 based on data-driven Bayesian inversions, which has recently been successfully applied to  
112 image the lithosphere at the scale of Western Europe (Nouibat et al., 2022). Specific and

113 careful pre-processing of OBS records is compulsory because they are affected by noise  
114 sources at the seabed such as compliance and tilting, and they may also be impacted by  
115 intrinsic instrumental noise (Crawford et al., 1998; Crawford & Webb, 2000; Deen et al.,  
116 2017). Furthermore, OBSs are sensitive to local noise sources such as tides and currents,  
117 boat traffic, or marine animals, which are not recorded coherently over long distances (e.g.,  
118 Batsi et al., 2019). Such noises are therefore unsuitable for ambient-noise tomography, and  
119 they even alter the signal-to-noise ratio of surface waves reconstructed by noise correlation.  
120 Finally, the water column above the seismometers (water depth of 1100 - 2800 m in our case)  
121 may have a significant impact on the quality of the Rayleigh-wave dispersion measurements  
122 between distant OBSs, particularly at periods shorter than 15 s. Wolf et al. (2021) have  
123 highlighted the difficulties in using the AASN OBSs to measure Rayleigh waves dispersion  
124 curves from noise correlations. These difficulties are partly related to the high level of sea-  
125 floor noises. To overcome these difficulties, we propose an innovative way of computing  
126 seismic noise correlations using OBS data that consist (1) in a pre-processing of the OBSs  
127 noise records that decrease efficiently the seabed noise, and (2) in computing iteratively  
128 noise correlations between OBS stations using onshore stations as virtual sources.

129 The overall methodology and its results are presented in sections 2 to 4. Section 2 is  
130 dedicated to the description of a specific pre-processing that aims at cleaning OBS daily  
131 noise records from instrumental transient glitches and seafloor noises. Section 3 presents  
132 how iterative noise correlations are computed between OBSs using onshore stations as vir-  
133 tual sources. In section 4, we show how noise correlations are used to build a 3-D  $S$ -wave  
134 velocity model of the Ligurian-Provence basin by computing 2-D probabilistic transdimen-  
135 sional Rayleigh wave group velocity maps and their uncertainties at different periods, and  
136 by inverting local dispersion curves to derive a probabilistic  $V_s$  model. The fifth and final  
137 section is dedicated firstly to a validation of the resulting 3-D  $V_s$  model through a compar-  
138 ison with a recent  $V_p$  model obtained along a linear refraction, wide-angle seismic profile in  
139 the center of the basin by Dannowski et al. (2020). Finally, we show how the combination  
140 of the  $V_p$  and  $V_s$  models along the same profile provides insightful clues to the structure and  
141 nature of the crust in the central Ligurian-Provence basin.

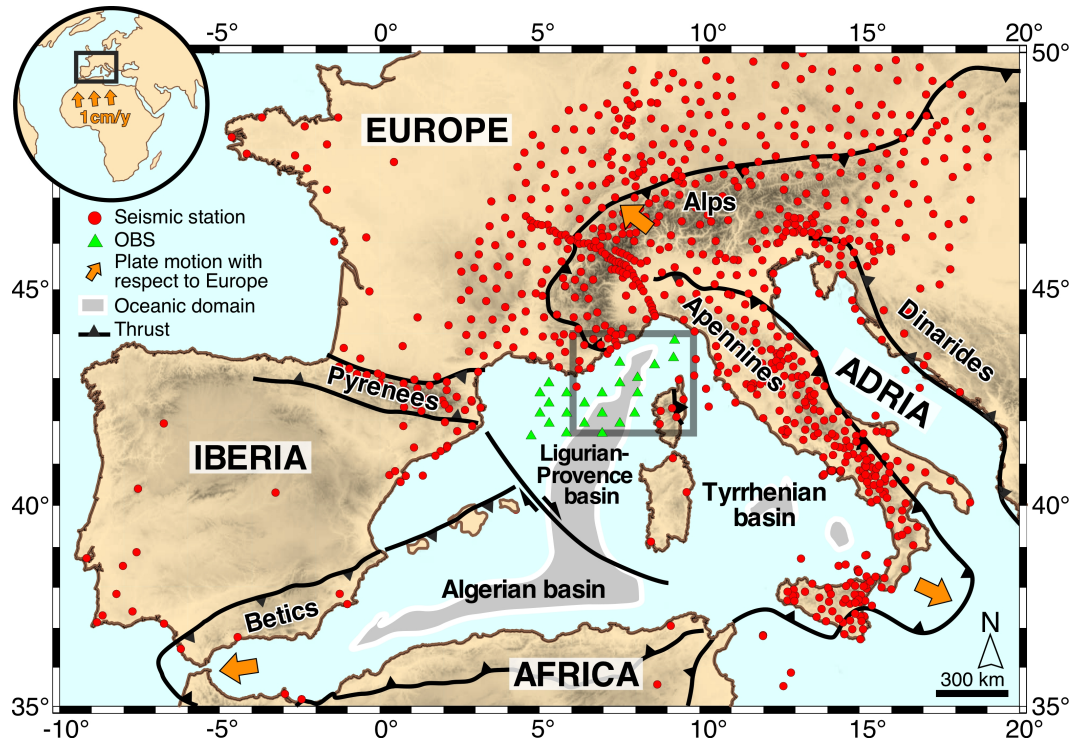


**Figure 1.** Tectonic map of the western Mediterranean region (modified from Faccenna et al., 2014; Jolivet et al., 2020) with locations of seismic stations used in this work (red circles: onshore sensors; green triangles: AASN OBS). The oceanic domains of the Ligurian-Provence, Algerian and Tyrrhenian back-arc basins are filled with gray color. The gray frame shows the location of the map in Figure 8a.

## 2 Data processing

### 2.1 Description of the AASN sea-bottom instruments

We processed ambient-noise records from 23 ocean-bottom-seismometers (OBS in Fig. 1) that were deployed for eight months in the northwestern Mediterranean Sea as the offshore part of the AlpArray temporary seismic network (AASN; network code Z3). All OBSs were deployed in June 2017 by the AlpArray-OBS cruise of the French R/V "Pourquoi-Pas?" (Crawford, 2017), and recovered in February 2018 by the MSM71 cruise of the German R/V "Maria S. Merian" (Kopp et al., 2018).

Sixteen LOBSTER instruments (Long-term Ocean Bottom Seismometer for Tsunami and Earthquake Research) belong to the GEOMAR and DEPAS pools (German instrument pool for amphibious seismology). Designed by K.U.M. Environmental- and Marine Technology GmbH, these instruments were equipped with HTI-01-PCA hydrophones from High Tech Inc., Trillium compact velocimeters from Nanometrics and K.U.M., and with CMG-40T velocimeters from Gralp for four of them. Seven broadband OBS (BBOBS) belong to the French OBS pool of INSU-IPGP. Designed by the Scripps Institution of Oceanography, these instruments were equipped with deep-sea differential pressure gauges and Nanometrics Trillium-240 very broadband velocimeters.

The drift of the sensor clocks was measured before the deployment and after the recovery. Recordings were then corrected for clock drift in the RESIF and GEOFON datacenters that archive and distribute the dataset. Hable et al. (2018) has demonstrated that the assumption of a linear clock drift is adequate for the ocean-bottom instruments used here.

### 2.2 Glitch removal

The first step of the processing of OBS data is the removal of instrumental transient nearly-periodic impulsive noises (glitches) from continuous records of the 7 French broadband OBSs (BBOBS in section 2.1). Indeed, the vertical-component signals exhibit glitches of 1-hr period caused by the activation of the hourly-check of the internal mass centering of the sensor. The pressure component exhibits glitches with a period of 2.65 hrs, related to data writing on the hard disk. No glitch was detected on the horizontal components. Similar glitches have been observed in other datasets recorded with the same instruments (e.g., Deen et al., 2017).

172 Similarly to Deen et al. (2017), we remove glitches from the data using an average  
173 glitch waveform matching algorithm. Detailed explanation can be found in Text S1 of the  
174 supporting information. Supplementary Fig. S1 shows a vertical-component daily record of  
175 OBS A416A before and after removing the hourly glitches. It documents the efficiency of the  
176 processing by comparing the original signal (in blue), the synthetic glitch signal time series  
177 (in red), and the final, glitch-free signal (in black). Similarly, Supplementary Fig. S2 shows  
178 a daily record of the pressure component before and after removing the 2.65-hrs-period  
179 glitches. The power spectral density curves of an example of 1-day raw and pre-processed  
180 vertical component record displayed in Fig. 2a, show that removing the glitches reduces the  
181 noise level by up to 15 dB at frequencies lower than  $10^{-1}$  Hz.

### 182 **2.3 Seafloor-noise reduction**

183 At frequencies below  $5 \times 10^{-2}$  Hz, the power spectral densities (PSD) of the three-  
184 component records of all OBSs are dominated by noise due to compliance and tilt (Fig. 2).  
185 The compliance is a long-period pressure signal generated by infra-gravity waves induced  
186 by pressure variations in the water column (Crawford et al., 1998). Tilting corresponds to  
187 displacements and rotations of the sensor induced by seafloor currents that also generate  
188 long-period noise. As documented by Fig. 2a, long-period noise is stronger on the horizontal  
189 components than on the vertical-component. Crawford and Webb (2000) have shown that  
190 noise on the vertical-component is lower when the instrument is better levelled. However,  
191 long-period noise on the vertical component strongly increases if the instrument is tilted,  
192 even slightly, since acceleration induced by seafloor currents on the horizontal components  
193 is projected onto the vertical component.

194 Tilt and compliance noises on the vertical-component records are reduced by using a  
195 frequency-dependent response function method (Crawford et al., 1998; Crawford & Webb,  
196 2000). The horizontal components are firstly corrected for compliance noise by subtracting  
197 coherent signals derived from the pressure component. In a second step, tilt noise is reduced  
198 in the vertical-component by subtracting coherent signals derived from the compliance-  
199 corrected horizontal components (black to green in Fig. 2a). Finally, the resulting vertical-  
200 component signal is corrected for compliance by subtracting the coherent signal derived from  
201 the pressure-component signal (green to purple). Text S2 of the supporting information  
202 provides a detailed explanation of this procedure.

203 Figure 2a shows the power spectral density of a daily, vertical-component record of OBS  
204 A416A before any correction is applied (blue curve), after correcting from the hourly glitches  
205 (black), from the tilt (green) and from the compliance (purple). As shown in Fig. 2b, the  
206 coherence of the raw vertical-component with the horizontal components (black and blue  
207 curves) increases below  $5 \times 10^{-2}$  Hz (see also Supplementary Fig. S3a) while coherence with  
208 the pressure component increases around  $1.2 \times 10^{-2}$  Hz. Figure 2a shows that the reduction  
209 of the tilt noise (green curve) is maximum (10 dB) at  $5 \times 10^{-3}$  Hz, which is the frequency with  
210 the maximum coherence between the vertical component and the 2 horizontal components.  
211 The correction for the compliance noise is almost negligible for this record except around  
212  $1.2 \times 10^{-2}$  Hz, where the coherence between the vertical and the pressure components  
213 increases (green area in Fig. 2b). Supplementary Fig. S3b confirms that the correction for  
214 compliance is maximized for this station around  $1.2 \times 10^{-2}$  Hz. In this specific case, the  
215 tilt noise is stronger than the compliance noise, which indicates that pressure variations  
216 generate less noise than sea-current induced tilt. This strong tilt noise may result from  
217 strong currents at the seabed and/or the presence of poorly consolidated sediments directly  
218 under the OBS. The lower compliance noise may be due to the large water depth of OBS  
219 A416A ( $\sim 2630$  m), damping the effect of pressure-induced infra-gravity waves.

### 220 3 Computation of noise correlations and group-velocity measurements

221 Once OBS records have been corrected for glitches and seafloor noises, we apply the  
222 same pre-processing scheme described below to the records of all stations, onshore and  
223 offshore, in order to prepare the calculation of inter-station cross-correlations. As explained  
224 in Soergel et al. (2020) and Nouibat et al. (2022), we first down-weight the contribution of  
225 earthquakes and other high-amplitude transients by removing all 4-hr segments with a peak  
226 amplitude 4 times greater than the standard deviation of the current daily record, and with  
227 a RMS greater than 1.5 times the daily mean RMS. Each daily record is then filtered into  
228 six period bands (3 - 5, 5 - 10, 10 - 20, 20 - 40, 40 - 80 and 80 - 200 s) and amplitudes are  
229 normalized by their envelope. Finally, the 6 filtered and normalized signals are stacked to  
230 obtain the 4-hr pre-processed broadband signal.

#### 231 3.1 First-order correlations

232 As in Nouibat et al. (2022), we compute seismic noise cross-correlations for all station  
233 pairs by segments of 4 hrs. The 4-hr correlations are normalized and stacked to obtain a

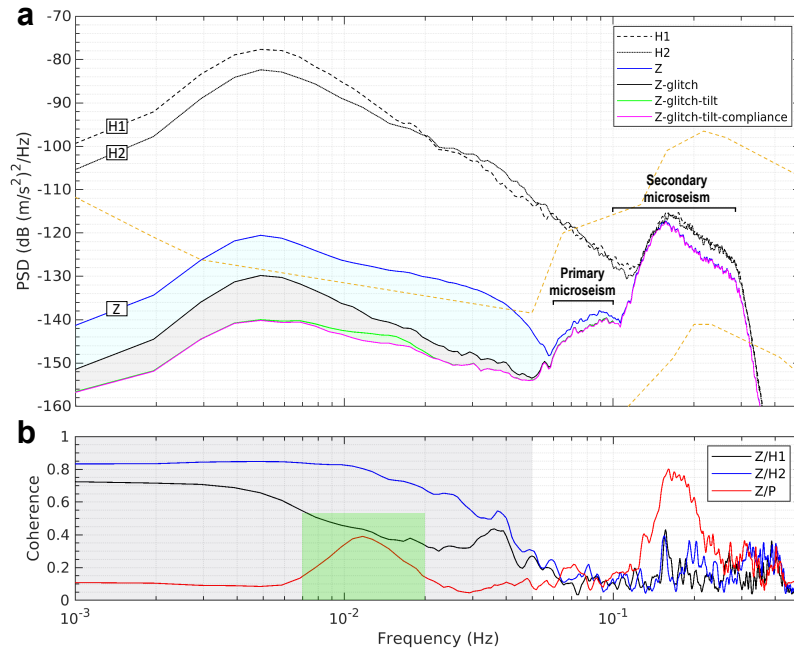


**Figure 2.** Effect of the different corrections for glitch and seafloor noises on the PSD of a 1-day vertical-component record of OBS A416A. Raw signals are band-pass filtered between 2.5 and 250 s, corrected from the instrumental response and decimated to 1 Hz sampling frequency. (a) PSDs before and after corrections; Orange dashed lines indicate the Peterson (1993) New Low and High Noise Model (NLNM & NHNM); Blue: PSD of the raw vertical-component record (blue signal in supplementary Fig. S1a); At frequencies  $> 5 \times 10^{-2}$  Hz, the PSD is dominated by the primary ( $\sim -140$  dB) and secondary ( $\sim -120$  dB) microseisms. At longer periods, the PSD is dominated by the effect of the periodic glitches and the seafloor noises with levels similar to the secondary microseism and higher than the NHNM (in the  $3 \times 10^{-3}$  Hz -  $4 \times 10^{-2}$  Hz band) with a peak amplitude at  $5 \times 10^{-3}$  Hz; Black: PSD of the Z-component after correction for the 1-hr glitches (black signal in supplementary Fig. S1a); The  $-130$  dB peak at  $5 \times 10^{-3}$  Hz remains, pointing to its oceanic origin; Its amplitude is weaker than the secondary microseism but still stronger than the primary microseism; Green: PSD of the Z-component after correction for the glitches and the tilt noise; Purple: PSD of the Z-component after correction for the glitches and seafloor noises; The maximum amplitude of the residual signal is now well below the primary microseism and the NHNM. The dotted and dashed black curves are the PSDs of the horizontal components. Colored areas show the reduction of the noise level after correcting from glitches (blue), from the tilt (gray), and from the compliance (green). (b) Coherence between the vertical channel and the horizontal (blue and black curves) and pressure (red curve) channels. The gray area shows the frequency domain where the Z-component is coherent with the horizontal components due to tilt noise. The green area shows the domain where the Z-component is coherent with the pressure component due to compliance noise. At frequencies higher than  $5 \times 10^{-2}$  Hz, the coherence is due to primary and secondary microseisms.

234 single reference correlation per station pair. We use up to 4 years of continuous vertical  
235 records for on-land stations pairs, and up to 8 months data to compute correlations for  
236 OBS-OBS and OBS-land-station pairs.

237 As shown by Nouibat et al. (2022) and supplementary Fig. S4a, Rayleigh waves are  
238 clearly visible in the correlations for on-land station pairs in a wide period band (5 - 150 s).  
239 The Rayleigh waves have an average signal-to-noise ratio (SNR) greater than 3.5 (Supple-  
240 mentary Table S1). Although correlations for OBS-land station pairs are computed from  
241 only 8 months of data, Rayleigh waves have a  $\text{SNR} > 3$  in the 5 - 70 s period band, except in  
242 the 40 - 70 s band where the SNR is slightly lower ( $\text{SNR} = 2.87$ , see supplementary Fig. S4b  
243 and Table S1). These noise correlations can therefore be used for Rayleigh-wave tomography.  
244 Supplementary Figures S4b-c demonstrate the effectiveness of corrections for glitches and  
245 seafloor noise in enhancing the SNR of correlations between OBS and land-station records.

246 First-order correlations between raw OBS records are displayed in the Fig. 3a. They  
247 can be compared to correlations for land-land station pairs and OBS-land station pairs  
248 shown in Supplementary Fig. S4. The SNR of correlation signals for OBS pairs is poorer  
249 than for other types of pairs in all period bands (average  $\text{SNR} < 2.6$ , Table 1). Therefore,  
250 Rayleigh waves are hardly detectable at periods shorter than 40 s in OBS-OBS correlations,  
251 and undetectable at longer periods ( $\text{SNR} < 1.6$ , Table 1). This may be explained by several  
252 factors such as local noises generated around the sensors by seafloor currents, or seismic  
253 noises generated between the stations that induce signals around time 0 s of the correlations,  
254 masking the Rayleigh waves. Therefore, these first-order OBS-OBS correlations of raw  
255 records cannot be used for Rayleigh-wave tomography.

256 Figure 3b and Table 1 document once again the effectiveness of the corrections for  
257 glitches and seafloor noises applied to OBS records, which improve the inter-OBS correlation  
258 signals. The correlations have a better SNR and are more symmetrical than those obtained  
259 from uncorrected signals, particularly at periods shorter than 40 s (columns a-b of Fig. 3).  
260 However, correlation signals are still noisy, particularly at short lag times, and accurate  
261 measurements of Rayleigh-wave group velocities remain challenging. To further improve  
262 the quality of correlations for OBS pairs, we chose to virtually reconstruct the Rayleigh  
263 waves by computing iterative correlations.

264

### 3.2 Iterative correlations for OBS-OBS paths

265

266

267

268

269

270

271

272

273

274

275

We have seen in the previous section that correlations for OBS pairs can hardly be used for Rayleigh-wave tomography. Since correlations computed between onshore stations and OBSs exhibit clear Rayleigh waves, we will use onshore stations as virtual sources in order to measure the travel time of Rayleigh waves between OBSs. Indeed, first-order correlations computed between onshore stations and OBSs contain the Rayleigh-wave part of the Green's function. It is thus possible to use them to mimic the case where Rayleigh waves are emitted on the continent and recorded by OBSs. By computing correlations of Rayleigh waves emitted by each virtual source and recorded by two OBSs (i.e., by computing a second-order correlation), it is possible, thanks to the stationary phase theorem, to isolate the Rayleigh-wave propagating between the two OBSs, and therefore to measure its travel time. We explain this with more detail in the following.

Let us consider any medium with a distribution of sources  $f$ . The wavefield recorded at a station  $A$  can be expressed using the Green's function  $G$  of the medium:

$$u(\vec{r}_A, t) = \int_{\Omega} \int_0^{\infty} G(\vec{r}_s, \vec{r}_A, t') f(\vec{r}_s, t - t') dt' d\vec{r}_s \quad (1)$$

It has been shown that the time-derivative of the first-order cross-correlation  $C_{\vec{r}_A, \vec{r}_B}^1(\tau)$  computed between wavefields recorded at two stations  $A$  and  $B$  is the Green's function  $G_{\vec{r}_A, \vec{r}_B}(t)$  of the medium, assuming for instance a perfectly homogeneous distribution of white noise everywhere in the medium (e.g., Lobkis & Weaver, 2001; Snieder, 2004; Wapenaar, 2004; Roux et al., 2005; Weaver, 2005; de Verdière, 2006):

$$\frac{d}{d\tau} C_{\vec{r}_A, \vec{r}_B}^1(\tau) = G_{\vec{r}_A, \vec{r}_B}(\tau) \quad (2)$$

In the case where all white noise sources are spatially uncorrelated, the correlation of wavefields recorded at  $A$  and  $B$  can be rewritten as the integral of correlations between  $G(\vec{r}, \vec{r}_A)$  and  $G(\vec{r}, \vec{r}_B)$ :

$$\begin{aligned} C^1(\vec{r}_A, \vec{r}_B, \tau) &= \int_0^{\infty} u(\vec{r}_A, t) u(\vec{r}_B, t + \tau) dt \\ &= \int_{\Omega} \int_0^{\infty} G(\vec{r}_s, \vec{r}_A, t') f(\vec{r}_s, t - t') dt' d\vec{r}_s \otimes \int_{\Omega} \int_0^{\infty} G(\vec{r}_s, \vec{r}_B, t') f(\vec{r}_s, t - t') dt' d\vec{r}_s \\ &= \int_{\Omega} G(\vec{r}_s, \vec{r}_A, t) \otimes G(\vec{r}_s, \vec{r}_B, t) d\vec{r}_s \end{aligned} \quad (3)$$

where  $\otimes$  denotes the cross-correlation operation. Since the time-derivative of correlations is similar to the Green's function of the medium, it follows immediately by substituting  $dC^1/dt$

to  $G$  in Eq. 3 that the first-order correlation is equivalent to a second-order correlation that we will note  $C^2$ :

$$C^1(r_A^{\vec{}}, r_B^{\vec{}}, \tau) = \int_{\Omega} \frac{d}{dt} C^1(r_s^{\vec{}}, r_A^{\vec{}}, t) \otimes \frac{d}{dt} C^1(r_s^{\vec{}}, r_B^{\vec{}}, t) dr_s^{\vec{}} = C^2(r_A^{\vec{}}, r_B^{\vec{}}, \tau) \quad (4)$$

Equation 4 indicates that it is possible to reconstruct the Green's function of the medium between  $A$  and  $B$  by re-correlating the noise correlations computed between each point of the medium and stations  $A$  and  $B$ . However, this demonstration assumes that the time-derivative of correlations are the exact and complete Green's function of the medium. The assumption would be correct if stations that could be used as virtual sources would exist everywhere in the medium.

In practice, the seismic noise recorded at the Earth surface in the period band considered in this work (5 - 150 s) is dominated by Rayleigh waves. As a consequence, noise correlations computed between onshore stations and OBSs do not provide the full Green's function of the medium including all propagating modes, but they do provide robust estimates of the travel time of Rayleigh waves.

Rather than attempting to reconstruct the full Green's function, we will measure the travel time of the Rayleigh waves between OBSs  $A$  and  $B$  by using a simplified approach inspired by Eq. 4. It consists in re-correlating only the Rayleigh-wave parts of the correlations computed between onshore stations and OBSs  $A$  and  $B$ , that we consider as the Rayleigh-wave part of the Green's function:

$$\begin{aligned} \frac{d}{d\tau} C^{2, Ray}(r_A^{\vec{}}, r_B^{\vec{}}, \tau) &= \frac{d}{d\tau} \int_{\Omega} \frac{d}{dt} C^{1, Ray}(r_s^{\vec{}}, r_A^{\vec{}}, t) \otimes \frac{d}{dt} C^{1, Ray}(r_s^{\vec{}}, r_B^{\vec{}}, t) dr_s^{\vec{}} \\ &\approx G^{Ray}(r_A^{\vec{}}, r_B^{\vec{}}, \tau) \end{aligned} \quad (5)$$

where superscript "Ray" indicates that we only correlate the fundamental mode of Rayleigh waves of first-order correlations. In that way, we only retrieve the fundamental mode of the Rayleigh-wave part of the Green's function.

In practice, the distribution of virtual sources is never homogeneous. Instead, we use land stations deployed all over Western Europe, while OBSs are located in the Ligurian Sea (Fig. 1). Therefore, the condition of the stationary phase theorem are not completely met. To circumvent this difficulty, we select virtual sources that are expected to contribute constructively to the correlations (Fig. 4). To that end, we design a virtual-source azimuthal-filter that only retains sources located in the end-fire lobe of the OBS couple, that is in azimuths at  $\pm 20^\circ$  with respect to the azimuth of the OBS pair. Moreover, we enhance the

297 virtual source coverage by using separately the causal and anticausal parts of the first-order  
298 correlations to compute the second-order correlation.

299 Because onshore stations are well distributed and OBS-onshore correlations exhibit  
300 clear Rayleigh waves, the use of virtual sources in iterative correlations for OBS-OBS paths  
301 leads to a higher quality of Rayleigh waveforms (columns b-c of Fig. 3 and Table 1). This is  
302 achieved through: (1) separately recovering the causal and anticausal parts of the Green's  
303 function by using separately the causal and anticausal parts of the first-order correlations,  
304 thus avoiding interferences at long periods, and (2) controlling the distribution of virtual  
305 sources, thus guaranteeing a higher quality of the  $C^2$ s by contrast to OBS-OBS  $C^1$ s that  
306 exhibit low signal-to-noise ratio probably due to local noise sources. These local noise  
307 sources do not contribute significantly to OBS-onshore stations paths, and therefore neither  
308 to second-order correlations. Supplementary Fig. S5 shows that phases of the Rayleigh  
309 waveforms reconstructed from the  $C^1$  and  $C^2$  processes match. In the 5 - 10 s band,  
310 iterative correlations do not systematically improve the signal quality as compared to first-  
311 order correlations. Therefore, we select for each path the correlation of highest quality after  
312 checking that the  $C^1$  and  $C^2$  are coherent.

313 The strengths of the iterative correlations make it possible to substantially improve  
314 the path coverage in the Ligurian-Provence domain (Table 1). Our results demonstrate  
315 the efficiency of this method in providing robust group-velocity measurements. Further  
316 illustration and validation will be the subject of a future paper.

### 317 3.3 Group-velocity measurements

318 Once first-order and iterative correlations have been computed for onshore and offshore  
319 stations respectively, we derive group-velocity dispersion curves of the causal and acausal  
320 parts of the correlations by using multiple filter analysis (MFA, Dziewonski et al., 1969;  
321 Herrmann, 1973). As in Nouibat et al. (2022), we adapt the width of the gaussian filter  
322 to the inter-station distance to accommodate the trade-off in resolution between the time  
323 and frequency domains (Levshin et al., 1989). We correct our group-velocity measurements  
324 from the biases that occur when the MFA method is applied on signals having a non-flat  
325 spectrum (Shapiro & Singh, 1999). This is especially important when measuring Rayleigh-  
326 wave velocities using noise correlations around the first and second microseismic peak, i.e.,  
327 around 7 s and 14 s.

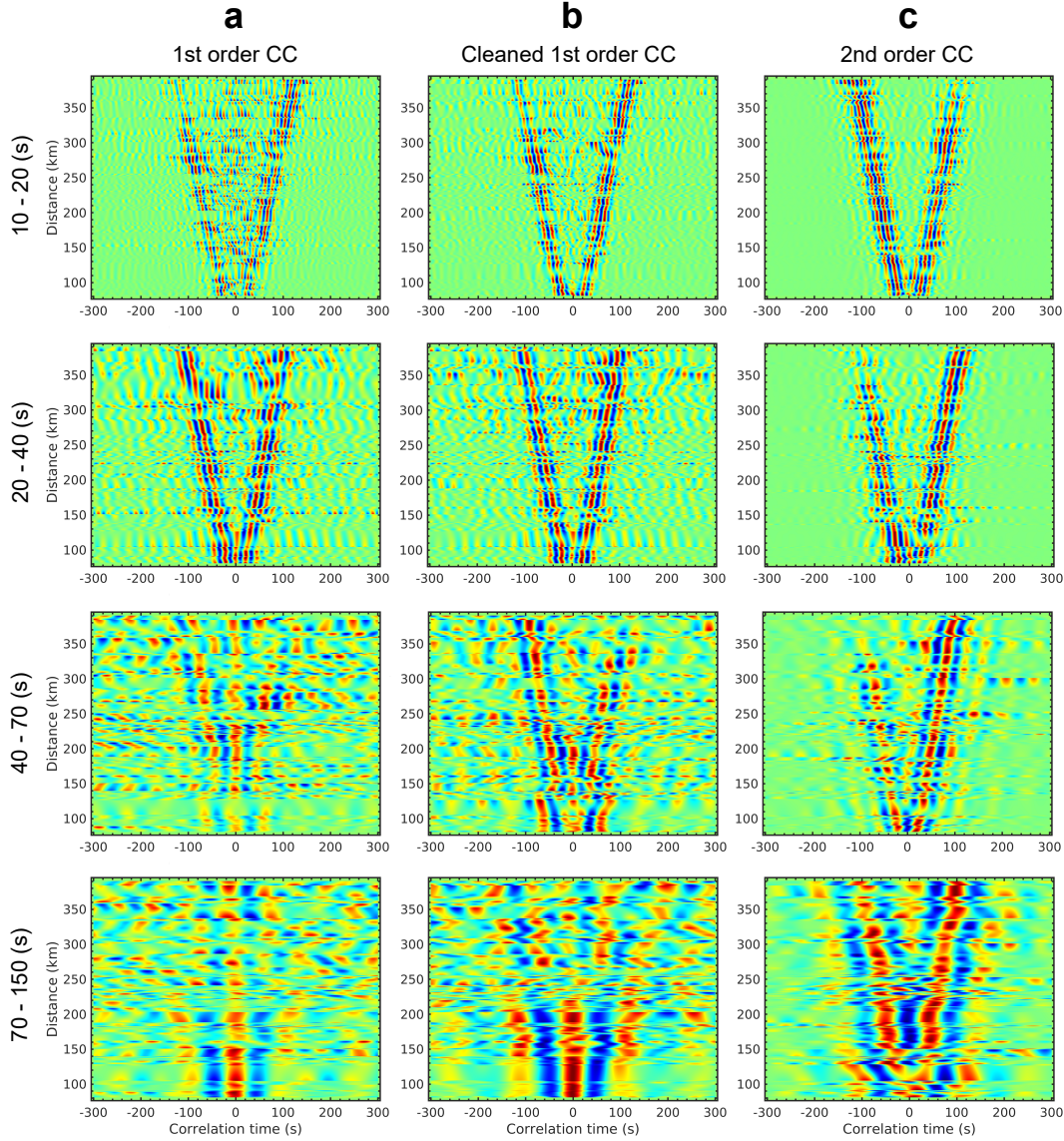


**Figure 3.** Time-distance plots of correlation signals for OBS-OBS pairs, obtained in different period bands at different steps of the processing. (a) First-order cross-correlations ( $C^1s$ ) of raw signals. (b)  $C^1s$  of pre-processed signals (glitch removal & seafloor-noise reduction). (c) Second-order correlations ( $C^2s$ ). The  $C^1s$  in (a) are generally of poor quality and poor symmetry, with strong signals at short lag times due to interferences even at short periods. These interferences become stronger with increasing period, and they progressively overshadow the Rayleigh wave-trains. In (b), the  $C^1$  signals are strongly improved due to corrections for glitches and seafloor noises, in particular in the three short- and medium-period bands. The 70 - 150 s band is still affected by interferences that hide the Rayleigh wave-trains. In (c), the quality and the time-symmetry of correlation signals are significantly improved in all period bands by the calculation of  $C^2s$ . In particular, the Rayleigh wave-train emerges from the noise in the long-period band.

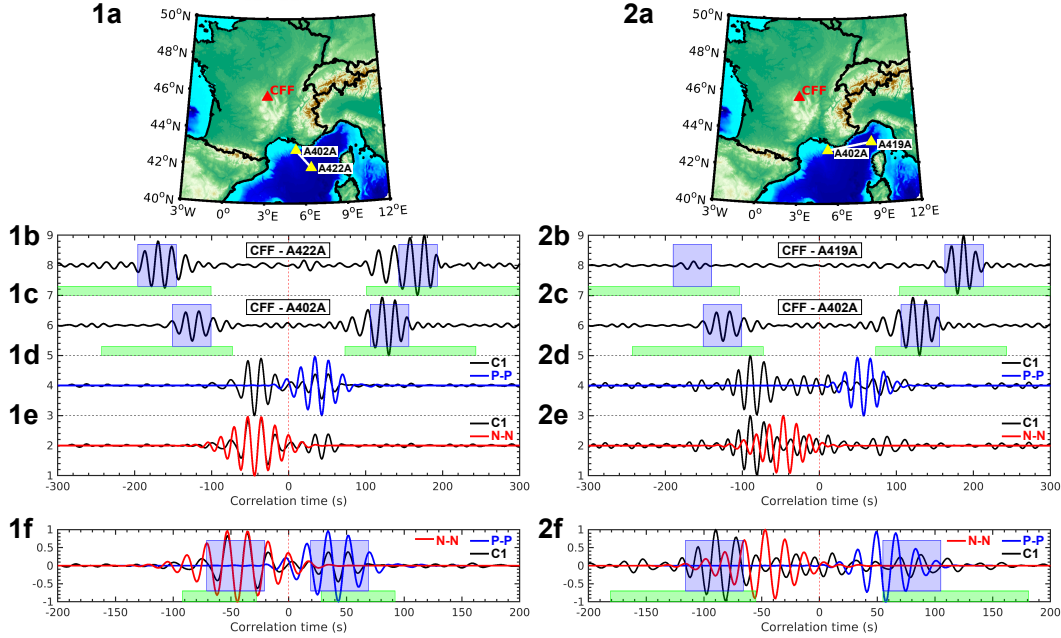


**Figure 4.** Details of the computation of second-order correlations for 2 examples of OBS-OBS pairs, using station CFF (FR network) as virtual source. (1-2a): Station location maps. In example (1), the virtual source is roughly aligned with the OBS pair, while in example (2), the azimuth of the virtual source is almost perpendicular to the pair. (1-2b, 1-2c): First-order correlation signals between CFF and each OBS. The green areas show the Rayleigh-wave search windows (wave propagation of 1 to 5 km/s over the inter-station distances). The blue areas show the Rayleigh-wave detection windows. (1-2d): First-order correlation of the OBS signals ( $C^1$ , in black), and correlation of the positive-time (causal) parts of the  $C^1$ s between CFF and the OBS couple (P-P, in blue). (1-2e): First-order correlation of the OBS signals ( $C^1$ , black), and correlation of the negative-time (acausal) parts of the  $C^1$ s between CFF and the OBS couple (N-N, red). (1-2f): Comparison of the causal (P-P, blue) and acausal (N-N, red)  $C^2$ s (that will be summed to obtain the final  $C^2$ ), with the first-order correlation of the OBS signals ( $C^1$ , black). The  $C^2$  and  $C^1$  signals have similar phases in (1) where the virtual source is aligned with the OBS pair. They have incoherent phases in (2), since CFF is not located in the end-fire lobe of this OBS pair (see text).

SNR — % of retained paths			
Period band	1st order CC	Cleaned 1st order CC	2nd order CC
10s – 20s	2.52 — 2.45%	3.29 — 8.11%	5.77 — 39.6%
20s – 40s	2.32 — 1.52%	3.61 — 11.5%	5.62 — 23.4%
40s – 70s	1.57 — 0.03%	3.12 — 5.22%	4.52 — 14.3%
70s – 150s	1.13 — 0.01%	1.42 — 2.61%	4.37 — 7.31%

**Table 1.** Signal-to-noise ratio and percentage of selected paths for group-velocity tomography in different period bands using: (1) first-order cross-correlations of raw OBS vertical-component records, (2) first-order cross-correlations of pre-processed signals (corrected for glitches, and seafloor noises), and (3) second-order cross-correlations of pre-processed signals.

328 In order to build the group-velocity maps in the Ligurian-Provence domain, we maxi-  
 329 mize the path coverage over the Ligurian Sea by using simultaneously OBS-OBS, land-land,  
 330 and land-OBS station pairs. A careful selection of group-velocity measurements is achieved  
 331 to keep the most reliable ones and discard those that are biased by an unfavorable distribu-  
 332 tion of noise sources, or by interferences of causal and acausal Rayleigh waves for instance.

333 For first-order correlations ( $C^1s$ ) computed between land-land and land-OBS stations,  
 334 at each period, we keep measurements if: (1) the SNR defined as the ratio of the Raleigh-  
 335 wave peak amplitude and the standard deviation of the following signal, is greater than 3  
 336 on the positive and negative correlation times, (2) group velocities measured in positive and  
 337 negative correlation times differ by less than 0.2 km/s, and (3) the inter-station distance  
 338 is greater than 2 wavelengths. For iterative correlations ( $C^2s$ ) computed between OBS  
 339 stations, we do not use the SNR criteria, since iterative correlations only exhibit the fun-  
 340 damental mode of the Rayleigh waves, owing to their construction. Nevertheless, for each  
 341  $C^2$  satisfying the distance and symmetry criteria, we only keep the group-velocity measure-  
 342 ment of the side of the correlation (positive or negative time) where the amplitude of the  
 343 Rayleigh-wave is maximum (i.e., where we have more virtual sources contributing).

344 Table 1 shows that for OBS-OBS pairs, the selection procedure would reject more than  
 345 97% of Rayleigh waves velocity measurements performed on first-order correlations com-  
 346 puted using OBS data that were not corrected from the compliance and tilt noises. This

347 illustrates that these signals are obviously not usable for ambient-noise tomography. By  
348 contrast, we selected between 2.6% to 11.5% of the measurements performed on first-order  
349 correlations done using OBS data corrected from sea floor noises. This highlights the im-  
350 portance of the pre-processing scheme described in section 2. Moreover, we kept between  
351 7.3% and 39.6% of group-velocity measurements performed on iterative correlations ( $C^2s$ )  
352 depending on the period-band considered. Second-order correlations provide a substantial  
353 gain over first-order correlations, leading to a significant improvement of the raypath cov-  
354 erage in the Ligurian-Provence basin with respect to the ANT of Wolf et al. (2021) based  
355 on first-order correlations.

## 356 4 3-D shear-wave velocity model

### 357 4.1 Inversion for 2-D group-velocity maps

358 We compute 2-D group-velocity maps and associated uncertainties using a "data-  
359 driven" transdimensional approach at discrete periods from 4 s to 150 s. At each period,  
360 probabilistic group-velocity maps are derived by exploring millions of 2-D models using the  
361 reversible-jump Markov-chain Monte-Carlo method (rj-McMC, Bodin et al., 2012). The  
362 method used for the inversion and the spatial resolution of the resulting group-velocity  
363 maps are discussed in detail in Nouibat et al. (2022). Uncertainty and path density maps  
364 at different periods are presented in Supplementary Figure S6.

365 Resulting group-velocity maps of the Ligurian-Provence basin and its margins are shown  
366 in Fig. 5 for periods from 6 s to 35 s. The 6 s and 8 s maps (sensitive to  $\sim 4 - 8$  km depth)  
367 highlight low-velocity anomalies ( $U < 1.6$  km/s) in the central and southwestern parts of  
368 the basin (C-SLPB in Fig. 5), that are probably associated with thick sediment sequences.  
369 These velocities are lower than those of the southeast-France basin and the Gulf of Lion  
370 (respectively SFB and GL in Fig. 5). The northeastern Ligurian-Provence basin (NLPB),  
371 its northern, Provence coast margin and its southern margin in Corsica have larger velocities  
372 ( $U \geq 2.4$  km/s). From simulations of Rayleigh-wave dispersion in synthetic 1-D models, we  
373 show that such periods are also highly sensitive to the presence and thickness of the water  
374 column (Supplementary Figure S7). The 10 s map still shows velocities lower than 2.5 km/s  
375 in the central and southwestern Ligurian-Provence basin. The 12 s and 15 s maps (sensitive  
376 to  $\sim 10 - 15$  km depths) highlight velocities larger than 3.5 km/s associated with the thin  
377 crust of the Ligurian basin. However, the northeastern basin has lower velocities indicative

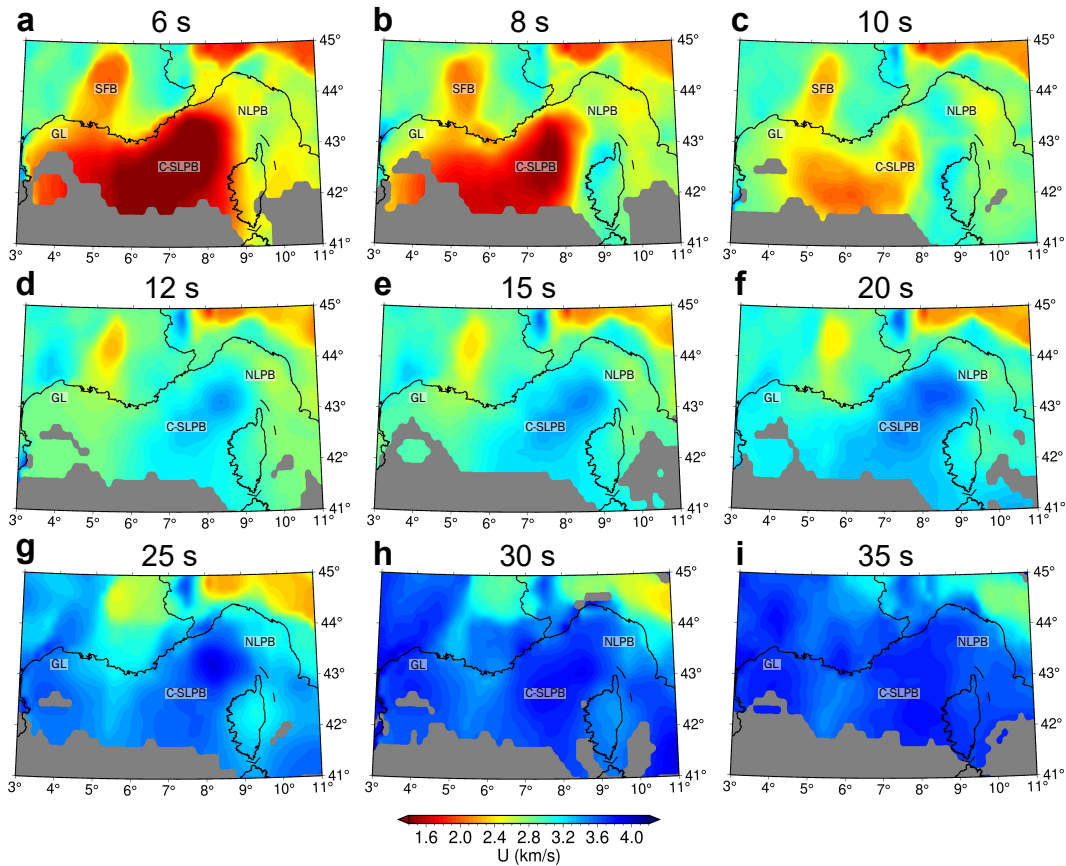


**Figure 5.** Group-velocity maps (average solutions) at 6 to 35 s periods, obtained with the Hierarchical Bayes reversible-jump algorithm. Only areas with uncertainty lower than  $0.5 \text{ km/s}$  are shown. C-SLPB: central and southwestern parts of the basin, GL: Gulf of Lion, NLPB: northeastern Ligurian-Provence basin, SFB: southeast-France basin.

of a deeper Moho in the Gulf of Genova. Velocities lower than  $3.2 \text{ km/s}$  correspond to thick crust under Corsica and the Provence coast. At 25 s period (sensitive to  $\sim 15 - 30 \text{ km}$  depth), velocities are still lower along the western coast of the Gulf of Genova than in the basin, indicative of a thicker crust, as in Corsica. At 30 s and 35 s periods, group velocities are homogeneous and exhibit large velocities ( $U > 3.5 \text{ km/s}$ ) in most of the study region.

#### 4.2 Inversion for shear-wave velocity

The group-velocity maps and their uncertainties are used to derive a 3-D  $V_s$  model. For this, we perform a two-step data-driven inversion to tackle the non-unicity of the inverse problem. The main part of this process is described in detail in Nouibat et al. (2022), so

387 we will only summarize it here. We will rather focus on the specificity of the inversion for  
388 the offshore region, which is the consideration of the water layer. A result of the inversion  
389 for  $V_s$  at an offshore location in the Ligurian Sea is shown in Supplementary Fig. S8.

390 Firstly, a 3-D probabilistic solution is computed that gives at each location the prob-  
391 ability distribution of  $V_s$  and the probability of having an interface as a function of depth.  
392 This is achieved using an exhaustive grid search on a set of  $\sim 130$  million synthetic four-layer  
393 models, which include a sedimentary layer, the upper crust, the lower crust and a half-space  
394 representing the upper mantle. The strength of this first-step Bayesian framework lies in  
395 constraining the structural complexity of the crust (i.e., of the short-period part of the  
396 dispersion curve) by means of an ensemble of models, fitting the dispersion curve to the  
397 degree required by its uncertainties. However, due to the four-layer model assumption, this  
398 procedure is not sufficient to fully describe the complexity of the model structure, particu-  
399 larly in the mantle part, that is in the long-period part of the dispersion curve. Hence, we  
400 use an iterative linear least-square inversion (Herrmann, 2013) as a complement to update  
401 the mantle part of the model and further refine the fit to the local dispersion curve for the  
402 crustal part (Supplementary Fig. S8).

403 The initial model for the linear inversion (second step) at a given location is the average  
404 of all selected probabilistic solutions of the first inversion step, weighted by their likelihood  
405 values. We discretize the crustal and mantle parts at intervals of 1 and 5 km, respectively,  
406 and assume a gradual increase of  $V_s$  below Moho according to the global model PREM  
407 (Dziewonski & Anderson, 1981). For offshore locations, we incorporate on top of this initial  
408 model an additional layer of thickness equal to water depth at the given location. The pa-  
409 rameters of this water layer are kept fixed during the linear least-square inversion (thickness,  
410  $V_s = 0$  km/s,  $V_p = 1.5$  km/s,  $\rho = 1 \times 10^3$  kg/m<sup>3</sup>). Since we invert for short periods as well,  
411 an appropriate parameterisation of the water column is crucial. Indeed, we highlight its  
412 influence by computing group-velocity dispersion curves for synthetic 3-layer crustal models  
413 representative of the oceanic crust of the Ligurian-Provence basin, and different water levels  
414 from 0 to 3.1 km (Supplementary Fig. S7). This shows that the effect of the water layer on  
415 the dispersion curve is substantial at periods shorter than 15 - 20 s, where the water depth  
416 changes impact: (1) the absolute group velocities, and (2) the shape of the dispersion curve,  
417 particularly in the vicinity of the Airy phase.

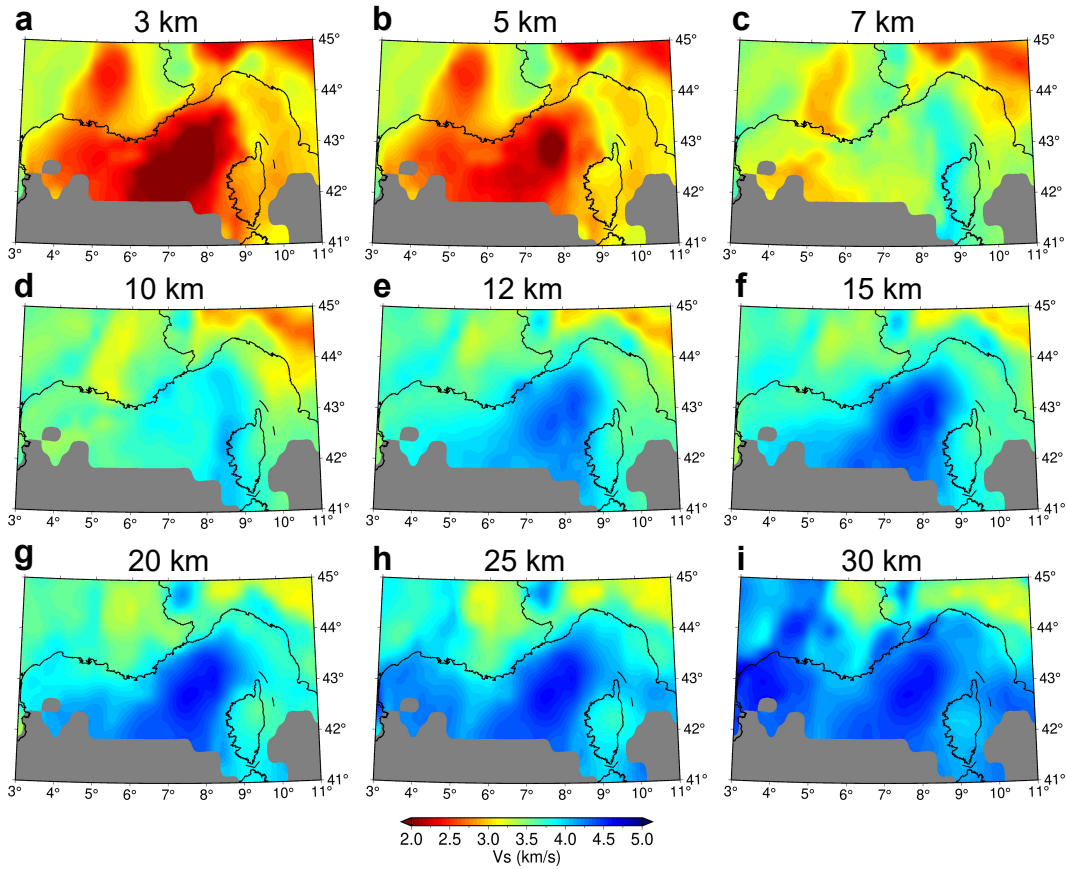


**Figure 6.** Depth slices in the final  $V_s$  model at 3 to 30 km depths. Only regions with  $1\sigma$  error  $< 8\%$  are shown.

418 Figure 6 shows depth slices in the 3-D shear-wave velocity model at 3 to 30 km depth.  
 419 The sediment layer is clearly visible at 3 - 7 km depth in the central and southwestern  
 420 Ligurian-Provence basin, with low velocities of 2 - 3.2 km/s. The transition from crustal  
 421 (3.5 - 4.1 km/s) to mantle velocities (4.1 - 4.5 km/s) is located between 10 km and 12 -  
 422 15 km in the parts of the basin with thinnest crust. Between 20 and 30 km, areas of strong  
 423 velocities corresponding to the mantle extend westward from the Ligurian-Provence basin  
 424 to the Gulf of Lion across a nearly N-S transition of slower velocities at  $\sim 5.5^\circ$  E.

### 4.3 Comparison with the $V_s$ model by Wolf et al. (2021)

425  
 426 Figure 7 shows a comparison of our  $V_s$  model and the model by Wolf et al. (2021),  
 427 which was the first published ambient-noise tomography using data of AlpArray OBSs in  
 This article is protected by copyright. All rights reserved.

428 the Ligurian basin. Our  $V_s$  model covers a wider area as part of the large-scale model by  
429 Nouibat et al. (2022) that uses all available broadband stations in Western Europe.

430 At 3-km depth, our model (Fig. 7-1a) highlights: (1) the sedimentary cover in the  
431 central and southwestern basin (1.8 - 2.2 km/s), where Wolf et al's model (Fig. 7-1b) exhibits  
432 patches of very low velocities ( $V_s \leq 1.4$  km/s), and (2) gradual increasing of velocity from the  
433 central basin towards the conjugate margins, which is not clearly visible in Wolf et al's model  
434 where velocities fluctuate from very low ( $V_s \leq 1.8$  km/s) to high values (2.4 - 2.5 km/s). At  
435 5-km depth, we still observe typical sediment velocities (Fig. 7-2a), while Wolf et al's model  
436 (Fig. 7-2b) exhibits higher velocities ( $V_s > 3.5$  km/s). At 13-km depth, our model (Fig. 7-  
437 3a) shows almost homogeneous mantle velocities in the basin ( $V_s \geq 4.1$  km/s) while Wolf et  
438 al's model (Fig. 7-3b) exhibits numerous small-size velocity anomalies, fluctuating between  
439 mantle-like ( $V_s \geq 4.1$  km/s) and crust-like velocities ( $V_s \leq 3.7$  km/s). These heterogeneities  
440 suggest a much more irregular Moho surface than in our model. At 20-km depth, our model  
441 (Fig. 7-4a) documents crustal thinning towards the basin axis with  $V_s$  increasing across the  
442 conjugate margins. Again, velocities in the central basin are more heterogeneous in Wolf et  
443 al's model (Fig. 7-4b), with localized small-size anomalies. Although the transition domain  
444 has an irregular shape in Wolf et al's model, it remains to first order similar to that shown  
445 in our model.

446 We think that such strong differences between the two  $V_s$  models are mostly due to  
447 differences in coverage and quality of Rayleigh-wave dispersion data. Indeed, we greatly  
448 enhanced the path coverage in the Ligurian basin by using iterative correlations for OBS-  
449 OBS paths. In addition, the use of all broadband stations in Western Europe provides  
450 long ray paths across the Ligurian sea, allowing us to improve path coverage to the west  
451 and southeast and make use of Rayleigh-wave dispersion measurements up to 150 s. On  
452 the other hand, Wolf et al. (2021) used only 23 onshore stations nearby the basin, thus a  
453 limited aperture. Therefore, they used earthquake records for periods greater than 20 s.  
454 To a lesser extent, the differences between the two models may also be explained by the  
455 different strategies used to invert Rayleigh-wave dispersion measurements. Wolf et al. (2021)  
456 computed their 2-D dispersion maps using a linear inversion that depends on an explicit  
457 regularization, while our transdimensional approach does not. Moreover, our 1-D Bayesian  
458 inversion for  $V_s$  take uncertainties on dispersion measurements into account, which is key  
459 for controlling model complexity.

460 As we will see in the following section, our  $V_s$  model is more coherent with current  
461 knowledge on the crustal structure of the Ligurian-Provence basin than the one by Wolf  
462 et al. (2021). In particular, the thickness of the sedimentary cover and Moho depth and  
463 geometry estimated from our  $V_s$  model are coherent with the  $V_p$  model by Dannowski et al.  
464 (2020) along the basin axis and with the stratigraphic log after Leprêtre et al. (2013).

## 465 5 Discussion

466 We now focus on the oceanic domain of the Ligurian-Provence basin (Fig. 8a), in  
467 particular on the comparison of our  $S$ -wave velocity model with a recent  $P$ -wave velocity  
468 model derived by Dannowski et al. (2020) from a controlled-source seismic profile recorded  
469 along the basin axis (thick black line in Fig. 8a). The availability of this high-resolution  
470  $V_p$  section provides a unique opportunity to assess the accuracy and validate our  $V_s$  model  
471 against an independent dataset. Moreover, the existence of  $V_p$  and  $V_s$  models along the same  
472 profile may provide clues on the petrological structure of the crust in the oceanic domain of  
473 the basin, which is still debated. Indeed, it has been proposed that the oceanic domain is  
474 made of an oceanic crust with a thin basaltic layer (e.g., Mascle & Rehault, 1990; Bonatti  
475 et al., 1990), or an exhumed and serpentinized mantle devoid of any volcanic upper layer  
476 (e.g., Boillot et al., 1989; Beslier et al., 1993; Jolivet et al., 2020), or even an hyper-extended  
477 continental crust (e.g., McKenzie, 1978; Pascal et al., 1993; Dannowski et al., 2020).

### 478 5.1 Geological setting of the Ligurian-Provence basin

479 The basin opening initiated at 30 Ma by a rifting phase between Europe and the  
480 Corsica-Sardinia block, as a result of back-arc extension above the Adria oceanic micro-  
481 plate, initially subducting north-westward (e.g., Faccenna et al., 1997). The progressive  
482 south-eastward roll-back and retreat of the Adria slab below the Corsica-Sardinia domain  
483 led to stretching of the continental crust followed by continental break-up during the early  
484 Miocene, and to the genesis of an oceanic crust between 20 and 15 Ma (Séranne, 1999).  
485 As a result, the Ligurian-Provence basin includes two thinned conjugate continental passive  
486 margins separated by an oceanic domain (Fig. 8a). According to Rollet et al. (2002), the  
487 entire region is characterized by magnetic anomalies, and by the presence of magmatic bodies  
488 identified from acoustic facies in seismic reflection profiles. The area between the margins  
489 and the oceanic domain is described as a transitional domain, likely made up of a very  
490 thin continental crust overlying a thick rift-related corner of magmatic underplating (e.g.,

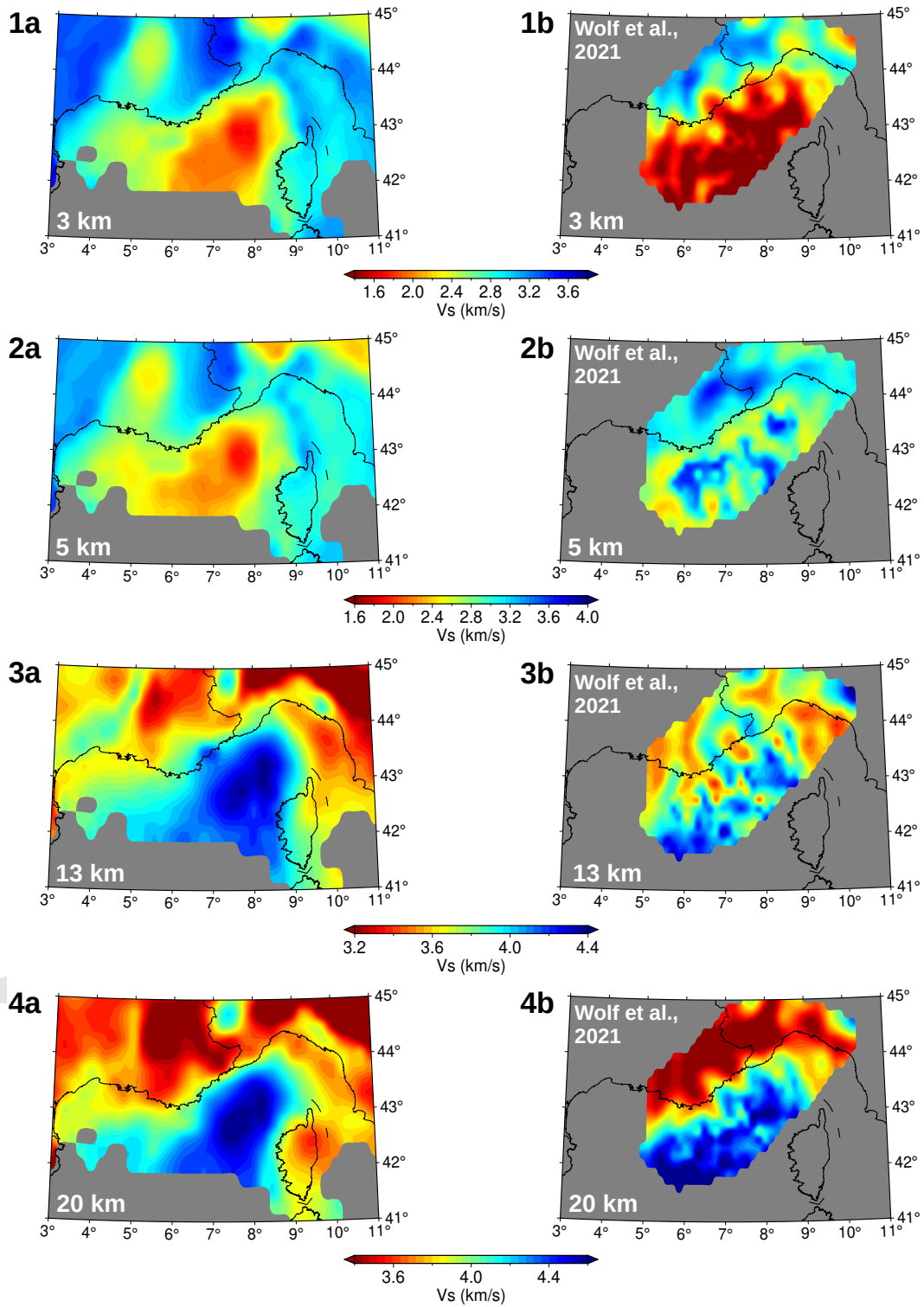


**Figure 7.** Comparison between our  $V_s$  model (left panel) and the  $V_s$  model by Wolf et al. (2021) (right panel) at four depths.

491 Séranne, 1999). This limit is marked by an abrupt change in the amplitude of magnetic  
492 anomalies with a transition from mostly positive values in the deep basin (i.e., oceanic  
493 domain) to negative values at the continent-ocean transition, and by a change in acoustic  
494 facies on seismic reflection profiles (e.g., Réhault et al., 1984; Déverchère & Beslier, 1995;  
495 Rollet et al., 2002). While the magmatism occurring in the margins has been associated to  
496 back-arc magmatic activity strongly influenced by subduction (e.g., Coulon, 1977; Bellon,  
497 1981; Réhault et al., 2012), the nature of magmatism observed in the oceanic domain remains  
498 unknown. It could not be investigated by direct geochemical analysis due to the presence  
499 of a sedimentary cover several kilometres thick.

500 Figure 8b shows a stratigraphic log representative of Western Mediterranean oceanic  
501 basins that includes  $P$ -wave velocity estimates. It is derived from the results of joint  
502 seismic wide-angle and reflection profiling in the Algerian and Western Sardinia basins  
503 (Klingelhoefer et al., 2008; Gailler et al., 2009; Leprêtre et al., 2013). The sedimentary layer  
504 of 5-*km* average thickness and 1.9 - 5 km/s  $P$ -wave velocities is made up of Plio-quaternary  
505 sediments, Messinian and pre-salt units (Fig. 8b). The transition from Plio-quaternary to  
506 Messinian units occurs at  $V_p \approx 2.5$  km/s. The Messinian sequence exhibits strong thick-  
507 ness variations ascribed to salt diapirism. It is separated from the pre-salt unit by the  
508 4.2 km/s velocity boundary. The deepest sediments overlay an oceanic basement that starts  
509 at  $V_p > 5$  km/s. The oceanic crust is relatively thin with an average thickness of 4.5 km. Its  
510  $P$ -wave velocities range from 5 to 7.2 - 7.3 km/s at  $\sim 12$  km depth, which corresponds to the  
511 Moho depth ( $V_p > 7.3$  km/s in the upper mantle). Controlled-source seismic data are useful  
512 to constrain the layer thicknesses and the depths of major interfaces (intra-sedimentary,  
513 sediment-crust and Moho), but their interpretation in terms of petrology only rely on  $P$ -  
514 wave velocity estimates. The interpretation is ambiguous as two lithologies of different  
515 petrological natures may have similar  $V_p$  (or  $V_s$ ) signatures. However,  $P$ - and  $S$ -wave ve-  
516 locities can be used jointly to yield information on lithologies and their hydration degree  
517 (e.g., Grevenmeyer et al., 2018; Malusà et al., 2021). For instance, the  $V_p/V_s$  ratio is com-  
518 monly used to assess the degree of serpentinization in oceanic domains and margins (e.g.,  
519 Bullock & Minshull, 2005; Reynard, 2013; Grevenmeyer et al., 2018). We will take advantage  
520 of the availability of the  $V_p$  cross-section by Dannowski et al. (2020) and our  $V_s$  section  
521 along the same profile to further constrain the petrological nature of the crust in the central  
522 Ligurian-Provence basin.

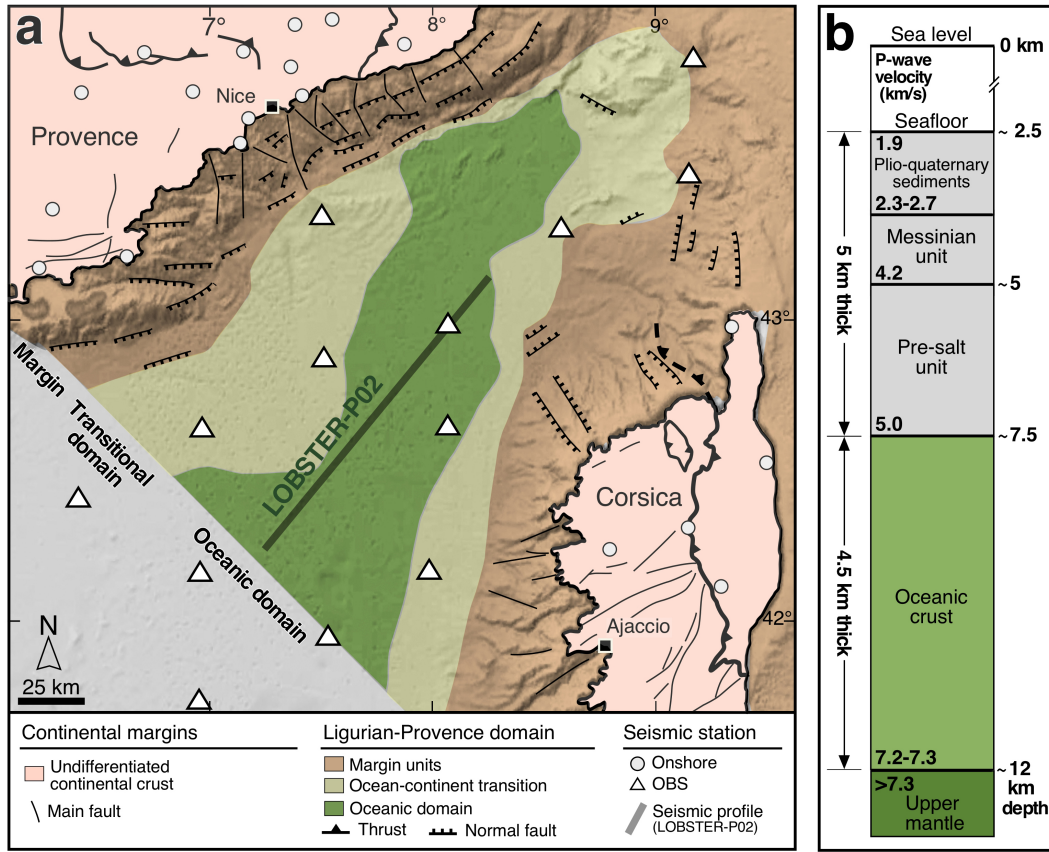


**Figure 8.** (a) Geological and tectonic setting of the Ligurian-Provence basin and European domains of southeast France and Corsica, showing: (1) continental margins, (2) transitional domains, and (3) the central oceanic domain. Gray line: trace of the seismic profile used in the discussion (Dannowski et al., 2020). Seismic stations are indicated by white triangles (AASN OBSs) and white circles (onshore stations). (b) stratigraphic log showing *P*-wave velocity and thickness of geological units observed in Western Mediterranean oceanic basins (after Leprêtre et al., 2013).

## 5.2 Seismic velocity cross-sections in the central oceanic domain

Figures 9a-b show vertical sections through our 3-D  $V_s$  model and probability of presence of interfaces along the SW-NE transect investigated by Dannowski et al. (2020). The  $P$ -wave velocity section of Dannowski et al. (2020) is shown in Fig. 9c.

Figure 9b shows two major layer boundaries at  $\sim 5$  and  $\sim 12$  km depth with rather high probabilities of presence, and a third one of weaker probability at  $\sim 7.5$  km depth. The good correspondence of the shallowest boundary with the velocity contour  $V_s = 2.5$  km/s suggests that it is probably an intra-sedimentary interface. This boundary also coincides with the 4.2 km/s  $P$ -wave velocity contour (Fig. 9c), which corresponds to the base of the Messinian salt unit according to Fig. 8b. This interpretation is consistent with  $S$ - and  $P$ -wave velocities, typical of salt (e.g., Yan et al., 2016). The intermediate interface at  $\sim 7.5$  km depth, which is slightly less pronounced than the Moho boundary (Fig. 9b) coincides with the velocity contours  $V_s = 3.5$  km/s (Fig. 9b) and  $V_p = 5$  km/s (Fig. 9c), which may support its interpretation as the sediment-crust boundary, in agreement with Fig. 8b. However, this interface does not correspond to a marked change in seismic velocity in the final model of Fig. 9a. Therefore, we cannot detect unambiguously the depth of the sediment-crust transition. We will use the proxy  $V_s = 3.5$  km/s (or  $V_p = 5$  km/s) for the sediment-crust boundary.

In the northeastern part of the transect ( $x > 70$  km), the lower crust has higher, but still crustal  $P$ -wave velocities (6.0 - 7.2 km/s, in green in Fig. 9c), hence a weaker  $P$ -wave velocity gradient at the Moho than in the southwestern part. By contrast,  $S$ -wave velocities are high and almost mantle-like (4.0 - 4.4 km/s), with a low  $S$ -wave velocity gradient at Moho depth, in particular at the northeastern end of the profile ( $x > 90$  km in Fig. 9a). These  $P$ - and  $S$ -wave velocities are typical of gabbro (Grevemeyer et al., 2018), which suggests a gabbro intrusive body within the oceanic crust. Our interpretation is at odds with Dannowski et al. (2020) who interpreted the high  $V_p$  part of the deep crust as hyper-extended continental crust based on gravity modeling. The observed high  $S$ -wave velocity rules out the continental crust hypothesis.

As outlined by Dannowski et al. (2020), the  $V_p = 7.2$  km/s is a good Moho proxy because it coincides with a very strong velocity gradient. In the southwestern part of the profile ( $x < 70$  km), the  $V_p = 7.2$  km/s contour closely corresponds to the  $V_s = 4.1$  km/s contour while it corresponds to the  $V_s = 4.4$  km/s contour for  $x > 70$  km, that is beneath the

555 gabbroic intrusion (Fig. 9c). Owing to the presence of the gabbro intrusion, a single  $S$ -wave  
556 velocity contour cannot be used as proxy for the petrological Moho in the Ligurian-Provence  
557 basin, unlike in continental areas (Nouibat et al., 2022).

558 In the southwestern part of the profile, the depths of the  $V_s$  (4.1 km/s) and  $V_p$  (7.2 km/s)  
559 Moho proxies differ by less than 1 km. Such a small discrepancy is remarkable, given that the  
560 two models are totally independent. The depth profiles of the two shallower layer boundaries  
561 are also remarkably similar to those of the  $V_p$  contours that define lithological layering in  
562 the western Mediterranean basins (Fig. 8b). Such similarity to the  $P$ -wave velocity model  
563 of Dannowski et al. (2020) validates the offshore part of our shear-wave velocity model, as  
564 similarity to the receiver function section of the Cifalps profile validated its onshore part  
565 (Nouibat et al., 2022).

566 In the few locations where information on  $P$ -wave velocity is available, the uppermost  
567 mantle has the seismic signature of a dry peridotite, with  $V_p > 7.2$  km/s and  $V_s > 4.0$  km/s  
568 (Grevemeyer et al., 2018). We find no evidence of serpentized mantle, which would show  
569 much lower  $P$ - and  $S$ -wave velocities. Dannowski et al. (2020) and Wolf et al. (2021) also  
570 concluded on low mantle serpentization in this part of the basin axis.

## 571 6 Conclusion

572 Using data of 23 ocean-bottom seismometers of the AlpArray network with those of 890  
573 temporary and permanent onshore stations, we have derived a 3-D high-resolution shear-  
574 wave velocity model encompassing the Ligurian-Provence basin and its conjugate margins.  
575 The OBS continuous records could be fully exploited after a careful, specific pre-processing  
576 scheme including removal of instrument noises (glitches) and reduction of seabed-induced  
577 compliance and tilt noises. We enhanced the quality of correlations between OBSs and  
578 maximized the path coverage in the Ligurian-Provence basin by involving correlations with  
579 onshore stations to virtually reconstruct Rayleigh waves propagating between OBSs. As in  
580 Nouibat et al. (2022), we computed 2-D group-velocity maps and their uncertainties using a  
581 data-driven transdimensional inversion of Rayleigh-wave group-velocity measurements. The  
582 dispersion data and their uncertainties have then been used jointly in a Bayesian probabilis-  
583 tic approach to derive a 3-D probabilistic shear-wave velocity model. The output average  
584 model was further refined using a linear inversion that accounts for the presence of the water  
585 column.

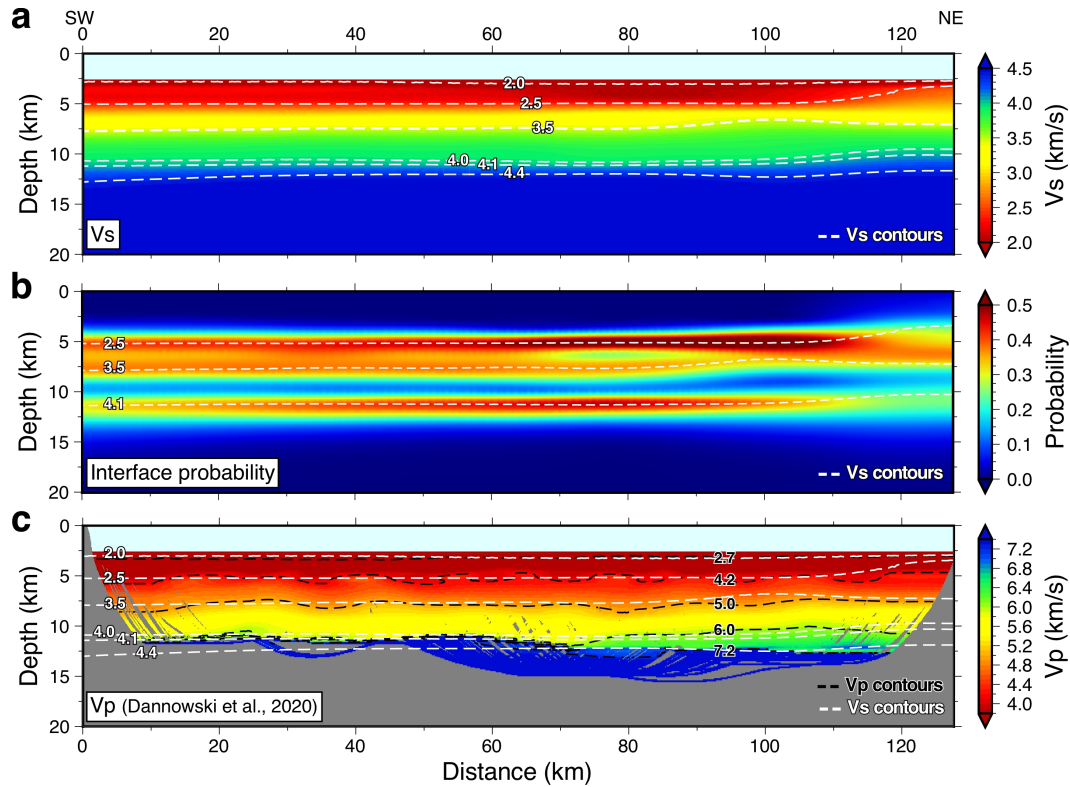


**Figure 9.** Depth sections along the LOBSTER-P02 transect (location shown in Fig. 8a). (a) Shear-wave velocities from our final model. The 2, 2.5, 3.5, 4, 4.1, and 4.4 km/s  $V_s$  contours are shown as white dashed lines. The water column is in sky blue. (b) Posterior probability densities of presence of a layer boundary obtained from the Bayesian inversion. White dashed lines indicate the 2.5, 3.5 and 4.1 km/s  $V_s$  contours. (c)  $P$ -wave velocities from Dannowski et al. (2020). Black dashed lines indicate the 2.7, 4.2, 5, 6, and 7.2 km/s  $V_p$  contours; white dashed lines as in (a).

586 The comparison with the high-resolution  $P$ -wave velocity section derived by Dannowski  
587 et al. (2020) from traveltimes inversion of controlled-source seismic data along the basin  
588 axis validates our 3-D ANT model. Layer boundaries revealed by high probabilities of  
589 presence of an interface and  $V_s$  contours are remarkably consistent with  $V_p$  contours. The  
590 joint interpretation of the  $V_p$  and  $V_s$  models highlights a relatively thin anomalous oceanic  
591 crust of low  $P$ -wave velocities but rather high  $S$ -wave velocities. In the NE part of the  
592 profile, the lower part of the crust exhibits a gabbroic intrusive body. The underlying  
593 mantle is anhydrous and shows no evidence of serpentinisation. These results show the  
594 potential of a joint interpretation of  $V_p$  and  $V_s$  models since they provide reliable answers  
595 to a number of debated questions on the petrological nature of the crust and uppermost  
596 mantle of the Ligurian-Provence basin, at least along the LOBSTER-P02 seismic profile.  
597 They also warrant the same type of study on the SEFASILS controlled-source seismic profile  
598 that crosses the northern margin of the basin (Dessa et al., 2020).

599 The use of OBS recordings in ambient-noise tomography is more challenging than with  
600 onshore stations due to shorter recording times, a higher potential of technical problems,  
601 sea-floor noises and generally a poorer signal-to-noise ratio in the frequency bands of micro-  
602 seismic noise that are key for ambient-noise tomography. Parts of these problems have been  
603 solved here by a specific pre-processing of OBS records that reduces instrument and sea-floor  
604 generated noises such as tilt and compliance. When available, land stations can be used in  
605 combination with OBSs to provide higher quality surface-wave signals between offshore and  
606 onshore stations than for OBS pairs, therefore improving interstation path coverage of ANT  
607 in particular at the ocean-continent transition. We went a step further by showing how to  
608 take full benefit of onshore stations to enhance the quality of correlations for OBS pairs.  
609 Our Rayleigh-wave reconstruction scheme for OBS pairs based on second-order correlations  
610 between OBSs and land stations has proven to be effective in improving the coverage of the  
611 offshore domain. Finally, the transdimensional inversion of the enhanced set of Rayleigh-  
612 wave group-velocity observations for group-velocity maps and their uncertainties and the  
613 following hybrid inversion for  $V_s$  that accounts for the water layer have led to a high-quality  
614 3-D  $V_s$  model of the study region. We have therefore set up a complete, efficient and reliable  
615 ambient-noise imaging methodology of oceanic domains and their margins using OBSs and  
616 land stations that opens new perspectives for the processing of similar datasets.

617 **Data availability statement**

618 Our tomographic 3-D model will be available in the Résif products repository (Réseau  
619 sismologique et géodésique Français; <https://www.resif.fr/en/data-and-products/products-repository/>). The inversion code is available on request to the first author.  
620

621 Waveform data used in this paper are available through the EIDA (European Integrated  
622 Data Archive) service of ORFEUS (<http://www.orfeus-eu.org/eida/>) and belong to the per-  
623 manent networks with codes AC, BE (Royal Observatory Of Belgium, 1985), CA (Institut  
624 Cartogràfic I Geològic De Catalunya - Institut D'Estudis Catalans, 1984), CH (Swiss Seis-  
625 mological Service (SED) At ETH Zurich, 1983), CR (University Of Zagreb, 2001), CZ  
626 (Institute Of Geophysics Of The Academy Of Sciences Of The Czech Republic, 1973), ES  
627 (Instituto Geografico Nacional, Spain, 1999), FR (RESIF, 1995), G (Institut de Physique  
628 du Globe de Paris (IPGP) & Ecole et Observatoire des Sciences de la Terre de Strasbourg  
629 (EOST), 1982), GB (GEOFON Data Centre, 1993), GR (Federal Institute for Geosciences &  
630 Natural Resources (BGR), 1976), IV (INGV Seismological Data Centre, 2006), NL (KNMI,  
631 1993), OE (ZAMG-Zentralanstalt Für Meteorologie Und Geodynamik, 1987), SL (Slovenian  
632 Environment Agency, 2001), and UP (SNSN, 1904). We also used data of the temporary Al-  
633 pArray network (network code Z3, AlpArray Seismic Network, 2015), Cifalps-2 experiments  
634 (network code XT, Zhao et al., 2018) and EASI experiments (network code XT, AlpArray  
635 Seismic Network, 2014).

636 **Acknowledgments**

637 This study was partly funded by the SEISCOPE consortium (<https://seiscope2.osug.fr/>),  
638 sponsored by AKERBP, CGG, CHEVRON, EQUINOR, EXXON-MOBIL, JGI, SHELL,  
639 SINOPEC, SISPROBE and TOTAL, and by the RGF program (Référentiel Géologique de  
640 la France, (<http://rgf.brgm.fr/>). It is part of the AlpArray-FR project funded by Agence  
641 Nationale de la Recherche (contract ANR-15-CE31-0015) and by Labex OSUG@2020 (In-  
642 vestissements d'Avenir, ANR-10-LABX-56). The deployment of OBSs for 8 months in the  
643 Liguro-Provençal basin was funded by project AlpArray-FR for the French component, and  
644 by the LOBSTER project that is part of the German Priority Programme SPP2017 4D-  
645 MB for the German component. This study was granted access to the HPC resources of  
646 the Dahu platform of the CIMENT infrastructure (<https://gricad.univ-grenoble-alpes.fr/>),  
647 which is supported by the Auvergne-Rhône-Alpes region (grant CPER07-13CIRA), the  
648 Labex OSUG@2020 (reference ANR10 LABX56) and the Equip@Meso project (reference

649 ANR-10-EQPX-29-01) of the program ‘Investissements d’Avenir’ supervised by the Agence  
650 Nationale de la Recherche and the HPC resources of CINES/IDRIS/TGCC under allocation  
651 046091 by GENCI. We warmly thank Aurélien Mordret for his constructive feedback on our  
652 inversion methodology and Anke Dannowski for providing us the P-wave velocity model. We  
653 are grateful to the operators of European permanent seismic networks who make their data  
654 available through EIDA (<http://www.orfeus-eu.org/data/eida/>). We are grateful to the  
655 captains and crews of R.V. Pourquoi Pas? (France) and R.V. Maria S. Merian (Germany)  
656 for their work during the AlpArray-Leg-1 deployment cruise (doi:10.17600/17000400) and  
657 the MSM71-LOBSTER recovery cruise (doi:10.3289/GEOMAR\_REP\_NS\_41\_2018). We also  
658 thank all members of the scientific crews, in particular C. Aubert, S. Besançon and R. Daniel.  
659 The DEPAS pool provided 16 sea-bottom instruments used in his work, while the INSU-  
660 IGP pool provided 7 broadband OBSs. The CIFALPS Team includes Coralie AUBERT,  
661 Elena EVA, Stéphane GUILLOT, Marco G. MALUSA, Silvia PONDRELLI, Simone SAL-  
662 IMBENI, Stefano SOLARINO, and Liang ZHAO. The Z3 network was operated by the  
663 AlpArray Seismic Network Team: György HETÉNYI, Rafael ABREU, Ivo ALLEGRETTI,  
664 Maria-Theresia APOLONER, Coralie AUBERT, Simon BESANÇON, Maxime BÈS DE  
665 BERC, Götz BOKELMANN, Didier BRUNEL, Marco CAPELLO, Martina ČARMAN,  
666 Adriano CAVALIERE, Jérôme CHÈZE, Claudio CHIARABBA, John CLINTON, Glenn  
667 COUGOULAT, Wayne C. CRAWFORD, Luigia CRISTIANO, Tibor CZIFRA, Ezio D’ALEMA,  
668 Stefania DANESI, Romuald DANIEL, Anke DANNOWSKI, Iva DASOVIĆ, Anne DE-  
669 SCHAMPS, Jean-Xavier DESSA, Cécile DOUBRE, Sven EGDORF, ETHZ-SED Electron-  
670 ics Lab, Tomislav FIKET, Kasper FISCHER, Wolfgang FRIEDERICH, Florian FUCHS,  
671 Sigward FUNKE, Domenico GIARDINI, Aladino GOVONI, Zoltán GRÁCZER, Gidera  
672 GRÖSCHL, Stefan HEIMERS, Ben HEIT, Davorka HERAK, Marijan HERAK, Johann  
673 HUBER, Dejan JARIĆ, Petr JEDLIČKA, Yan JIA, Hélène JUND, Edi KISSLING, Stefan  
674 KLINGEN, Bernhard KLOTZ, Petr KOLÍNSKÝ, Heidrun KOPP, Michael KORN, Josef  
675 KOTEK, Lothar KÜHNE, Krešo KUK, Dietrich LANGE, Jürgen LOOS, Sara LOVATI,  
676 Deny MALENGROS, Lucia MARGHERITI, Christophe MARON, Xavier MARTIN, Marco  
677 MASSA, Francesco MAZZARINI, Thomas MEIER, Laurent MÉTRAL, Irene MOLINARI,  
678 Milena MORETTI, Anna NARDI, Jurij PAHOR, Anne PAUL, Catherine PÉQUEGNAT,  
679 Daniel PETERSEN, Damiano PESARESI, Davide PICCININI, Claudia PIROMALLO,  
680 Thomas PLENEFISCH, Jaroslava PLOMEROVÁ, Silvia PONDRELLI, Snježan PREVOL-  
681 NIK, Roman RACINE, Marc RÉGNIER, Miriam REISS, Joachim RITTER, Georg RÜMPKER,

682 Simone SALIMBENI, Marco SANTULIN, Werner SCHERER, Sven SCHIPPKUS, Detlef  
 683 SCHULTE-KORTNACK, Vesna ŠIPKA, Stefano SOLARINO, Daniele SPALLAROSSA,  
 684 Kathrin SPIEKER, Josip STIPČEVIĆ, Angelo STROLLO, Bálint SÜLE, Gyöngyvér SZANYI,  
 685 Eszter SZŰCS, Christine THOMAS, Martin THORWART, Frederik TILMANN, Stefan  
 686 UEDING, Massimiliano VALLOCCHIA, Luděk VECSEY, René VOIGT, Joachim WASSER-  
 687 MANN, Zoltán WÉBER, Christian WEIDLE, Viktor WESZTERGOM, Gauthier WEY-  
 688 LAND, Stefan WIEMER, Felix WOLF, David WOLYNIEC, Thomas ZIEKE, Mladen ŽIVČIĆ,  
 689 Helena ŽLEBČÍKOVÁ.

## 690 References

- 691 Alder, C., Debayle, E., Bodin, T., Paul, A., Stehly, L., Pedersen, H., & the AlpArray Work-  
 692 ing Group. (2021, 02). Evidence for radial anisotropy in the lower crust of the Apen-  
 693 nines from Bayesian ambient noise tomography in Europe. *Geophysical Journal Inter-*  
 694 *national*, *226*(2), 941-967. Retrieved from <https://doi.org/10.1093/gji/ggab066>  
 695 doi: 10.1093/gji/ggab066
- 696 AlpArray Seismic Network. (2014). *Eastern Alpine Seismic Investigation (EASI) - Al-*  
 697 *pArray Complimentary Experiment*. AlpArray Working Group. doi: [https://doi.org/](https://doi.org/10.12686/alparray/xt_2014)  
 698 [10.12686/alparray/xt\\_2014](https://doi.org/10.12686/alparray/xt_2014)
- 699 AlpArray Seismic Network. (2015). *AlpArray Seismic Network (AASN) temporary compo-*  
 700 *nent*. AlpArray Working Group. doi: [10.12686/ALPARRAY/Z3\\_2015](https://doi.org/10.12686/ALPARRAY/Z3_2015)
- 701 Batsi, E., Tsang-Hin-Sun, E., Klingelhoefer, F., Bayrakci, G., Chang, E. T., Lin, J.-Y., ...  
 702 Géli, L. (2019). Nonseismic signals in the ocean: Indicators of deep sea and seafloor  
 703 processes on ocean-bottom seismometer data. *Geochemistry, Geophysics, Geosystems*,  
 704 *20*(8), 3882-3900. Retrieved from [https://agupubs.onlinelibrary.wiley.com/](https://agupubs.onlinelibrary.wiley.com/doi/abs/10.1029/2019GC008349)  
 705 [doi/abs/10.1029/2019GC008349](https://doi.org/10.1029/2019GC008349) doi: <https://doi.org/10.1029/2019GC008349>
- 706 Bayer, R., Le Mouel, J., & Le Pichon, X. (1973). Magnetic anomaly pattern in the western  
 707 mediterranean: Earth and planetary sci. *Letters*, *19*(2), 168–176.
- 708 Bellon, H. (1981). Chronologie radiométrique (k-ar) des manifestations magmatiques autour  
 709 de la méditerranée occidentale entre 33 et 1 ma. In *Consiglio nazionale delle ricerche.*  
 710 *international conference* (pp. 341–360).
- 711 Beslier, M.-O., Ask, M., & Boillot, G. (1993). Ocean-continent boundary in the iberia  
 712 abyssal plain from multichannel seismic data. *Tectonophysics*, *218*(4), 383–393.
- 713 Bodin, T., Sambridge, M., Rawlinson, N., & Arroucau, P. (2012, 06). Transdimensional

- 714 tomography with unknown data noise. *Geophysical Journal International*, 189(3),  
 715 1536-1556. Retrieved from <https://doi.org/10.1111/j.1365-246X.2012.05414.x>  
 716 doi: 10.1111/j.1365-246X.2012.05414.x
- 717 Boillot, G., Féraud, G., Recq, M., & Girardeau, J. (1989). Undercrusting by serpentinite  
 718 beneath rifted margins. *Nature*, 341(6242), 523–525.
- 719 Bonatti, E., Seyler, M., Channell, J., Girardeau, J., & Mascle, G. (1990). Peridotites  
 720 drilled from the tyrrhenian sea, odp leg 107. In *Proc. ocean drill. program sci. results*  
 721 (Vol. 107, pp. 37–47).
- 722 Bullock, A. D., & Minshull, T. A. (2005, 11). From continental extension to seafloor  
 723 spreading: crustal structure of the Goban Spur rifted margin, southwest of the UK.  
 724 *Geophysical Journal International*, 163(2), 527-546. Retrieved from [https://doi](https://doi.org/10.1111/j.1365-246X.2005.02726.x)  
 725 [.org/10.1111/j.1365-246X.2005.02726.x](https://doi.org/10.1111/j.1365-246X.2005.02726.x) doi: 10.1111/j.1365-246X.2005.02726.x
- 726 Coulon, C. (1977). Le volcanisme calco-alkalin cénozoïque de sardaigne (italie):  
 727 Pétrologie, géochimie et genese des laves andésitiques et des ignimbrites: Significa-  
 728 tion géodynamique, these de doctorat. *Univ. d'Aix-Marseille III, Aix en Provence,*  
 729 *France.*
- 730 Crawford, W. (2017). AlpArray LEG1 cruise, RV Pourquoi pas ?  
 731 doi: 10.17600/17000400
- 732 Crawford, W., & Webb, S. (2000). Identifying and removing tilt noise from low-frequency (i  
 733 0.1 hz) seafloor vertical seismic data. *Bulletin of the Seismological Society of America*,  
 734 90(4), 952–963.
- 735 Crawford, W., Webb, S., & Hildebrand, J. (1998). Estimating shear velocities in the oceanic  
 736 crust from compliance measurements by two-dimensional finite difference modeling.  
 737 *Journal of Geophysical Research: Solid Earth*, 103(B5), 9895-9916. doi: [https://](https://doi.org/10.1029/97JB03532)  
 738 [doi.org/10.1029/97JB03532](https://doi.org/10.1029/97JB03532)
- 739 Dannowski, A., Kopp, H., Grevemeyer, I., Lange, D., Thorwart, M., Bialas, J., & Wollatz-  
 740 Vogt, M. (2020). Seismic evidence for failed rifting in the ligurian basin, western alpine  
 741 domain. *Solid Earth*, 11(3), 873–887. Retrieved from [https://se.copernicus.org/](https://se.copernicus.org/articles/11/873/2020/)  
 742 [articles/11/873/2020/](https://se.copernicus.org/articles/11/873/2020/) doi: 10.5194/se-11-873-2020
- 743 Deen, M., Wielandt, E., Stutzmann, E., Crawford, W., Barruol, G., & Sigloch,  
 744 K. (2017). First Observation of the Earth's Permanent Free Oscillations  
 745 on Ocean Bottom Seismometers. *Geophysical Research Letters*, 44(21), 10,988-  
 746 10,996. Retrieved from <https://agupubs.onlinelibrary.wiley.com/doi/abs/10>

- 747 .1002/2017GL074892 doi: <https://doi.org/10.1002/2017GL074892>
- 748 Dessa, J.-X., Beslier, M.-O., Schenini, L., Chamot-Rooke, N., Corradi, N., Delescluse, M.,  
 749 ... others (2020). Seismic exploration of the deep structure and seismogenic faults  
 750 in the ligurian sea by joint multi channel and ocean bottom seismic acquisitions:  
 751 Preliminary results of the sefasils cruise. *Geosciences*, *10*(3), 108.
- 752 de Verdière, Y. C. (2006). Mathematical models for passive imaging i: general background.  
 753 *arXiv: Mathematical Physics*.
- 754 Dziewonski, A., & Anderson, L. (1981). Preliminary reference earth model. *Physics of the*  
 755 *earth and planetary interiors*, *25*(4), 297–356.
- 756 Dziewonski, A., Bloch, S., & Landisman, M. (1969, 02). A technique for the analysis  
 757 of transient seismic signals. *Bulletin of the Seismological Society of America*, *59*(1),  
 758 427-444.
- 759 Déverchère, J., & Beslier, M.-O. (1995). Malis cruise, rv le nadir.  
 760 doi: <https://doi.org/10.17600/95000010>
- 761 Egger, A., Demartin, M., Ansorge, J., Banda, E., & Maistrello, M. (1988). The gross  
 762 structure of the crust under corsica and sardinia. *Tectonophysics*, *150*, 363-389.
- 763 Faccenna, C., Becker, T. W., Auer, L., Billi, A., Boschi, L., Brun, J. P., ... Serpelloni,  
 764 E. (2014). Mantle dynamics in the mediterranean. *Reviews of Geophysics*, *52*(3),  
 765 283-332. Retrieved from [https://agupubs.onlinelibrary.wiley.com/doi/abs/10](https://agupubs.onlinelibrary.wiley.com/doi/abs/10.1002/2013RG000444)  
 766 [.1002/2013RG000444](https://doi.org/10.1002/2013RG000444) doi: <https://doi.org/10.1002/2013RG000444>
- 767 Faccenna, C., Mattei, M., Funicello, R., & Jolivet, L. (1997). Styles of back-arc extension  
 768 in the central mediterranean. *Terra Nova*, *9*(3), 126-130. Retrieved from [https://](https://onlinelibrary.wiley.com/doi/abs/10.1046/j.1365-3121.1997.d01-12.x)  
 769 [onlinelibrary.wiley.com/doi/abs/10.1046/j.1365-3121.1997.d01-12.x](https://onlinelibrary.wiley.com/doi/abs/10.1046/j.1365-3121.1997.d01-12.x) doi:  
 770 <https://doi.org/10.1046/j.1365-3121.1997.d01-12.x>
- 771 Federal Institute for Geosciences, & Natural Resources (BGR). (1976). German Regional  
 772 Seismic Network (GRSN). Retrieved 2020-08-20, from [https://www.seismologie](https://www.seismologie.bgr.de/doi/grsn/)  
 773 [.bgr.de/doi/grsn/](https://www.seismologie.bgr.de/doi/grsn/) (Publisher: Federal Institute for Geosciences and Natural Re-  
 774 sources (BGR)) doi: 10.25928/MBX6-HR74
- 775 Gailler, A., Klingelhoefer, F., Olivet, J.-L., Aslanian, D., Technical, O., et al. (2009). Crustal  
 776 structure of a young margin pair: New results across the liguro–provencal basin from  
 777 wide-angle seismic tomography. *Earth and Planetary Science Letters*, *286*(1-2), 333–  
 778 345.

- 779 GEOFON Data Centre. (1993). GEOFON seismic network. Retrieved 2020-08-20,  
780 from <http://geofon.gfz-potsdam.de/doi/network/GE> (Publisher: Deutsches Ge-  
781 oForschungsZentrum GFZ) doi: 10.14470/TR560404
- 782 Grevemeyer, I., Hayman, N. W., Peirce, C., Schwardt, M., Van Avendonk, H. J., Dan-  
783 nowski, A., & Papenberg, C. (2018). Episodic magmatism and serpentized mantle  
784 exhumation at an ultraslow-spreading centre. *Nature Geoscience*, *11*(6), 444–448.
- 785 Gueguen, E., Doglioni, C., & Fernandez, M. (1998). On the post-25 ma geo-  
786 dynamic evolution of the western mediterranean. *Tectonophysics*, *298*(1), 259-  
787 269. Retrieved from [https://www.sciencedirect.com/science/article/pii/](https://www.sciencedirect.com/science/article/pii/S0040195198001899)  
788 S0040195198001899 doi: [https://doi.org/10.1016/S0040-1951\(98\)00189-9](https://doi.org/10.1016/S0040-1951(98)00189-9)
- 789 Hable, S., Sigloch, K., Barruol, G., Stähler, S. C., & Hadziioannou, C. (2018, 06). Clock  
790 errors in land and ocean bottom seismograms: high-accuracy estimates from multiple-  
791 component noise cross-correlations. *Geophysical Journal International*, *214*(3), 2014-  
792 2034. Retrieved from <https://doi.org/10.1093/gji/ggy236> doi: 10.1093/gji/  
793 ggy236
- 794 Hable, S., Sigloch, K., Stutzmann, E., Kiselev, S., & Barruol, G. (2019, 07). Tomography of  
795 crust and lithosphere in the western Indian Ocean from noise cross-correlations of land  
796 and ocean bottom seismometers. *Geophysical Journal International*, *219*(2), 924-944.  
797 Retrieved from <https://doi.org/10.1093/gji/ggz333> doi: 10.1093/gji/ggz333
- 798 Harmon, N., Forsyth, D., & Webb, S. (2007). Using ambient seismic noise to determine  
799 short-period phase velocities and shallow shear velocities in young oceanic lithosphere.  
800 *Bulletin of the Seismological Society of America*, *97*(6), 2009–2023.
- 801 Herrmann, R. B. (1973, 04). Some aspects of band-pass filtering of surface waves. *Bulletin*  
802 *of the Seismological Society of America*, *63*(2), 663-671. Retrieved from [https://](https://doi.org/10.1785/BSSA0630020663)  
803 [doi.org/10.1785/BSSA0630020663](https://doi.org/10.1785/BSSA0630020663) doi: 10.1785/BSSA0630020663
- 804 Herrmann, R. B. (2013, 11). Computer Programs in Seismology: An Evolving Tool for  
805 Instruction and Research. *Seismological Research Letters*, *84*(6), 1081-1088. Retrieved  
806 from <https://doi.org/10.1785/0220110096> doi: 10.1785/0220110096
- 807 Hetényi, G., Molinari, I., & Clinton, J. (2018, 09). The AlpArray Seismic Network: A Large-  
808 Scale European Experiment to Image the Alpine Orogen. *Surveys in Geophysics*, *39*.  
809 doi: 10.1007/s10712-018-9472-4
- 810 INGV Seismological Data Centre. (2006). Rete Sismica Nazionale (RSN). Retrieved  
811 2020-08-20, from <http://cnt.rm.ingv.it/instruments/network/IV> (Publisher:

- 812 Istituto Nazionale di Geofisica e Vulcanologia (INGV), Italy) doi: 10.13127/SD/  
 813 X0FXNH7QFY
- 814 Institut Cartogràfic I Geològic De Catalunya - Institut D'Estudis Catalans. (1984). *Catalan*  
 815 *Seismic Network*. Retrieved 2019-02-08, from [http://www.fdsn.org/doi/10.7914/](http://www.fdsn.org/doi/10.7914/SN/CA)  
 816 [SN/CA](http://www.fdsn.org/doi/10.7914/SN/CA) (Publisher: International Federation of Digital Seismograph Networks) doi:  
 817 10.7914/SN/CA
- 818 Institut de Physique du Globe de Paris (IPGP), & Ecole et Observatoire des Sciences de la  
 819 Terre de Strasbourg (EOST). (1982). *GEOSCOPE, French Global Network of broad*  
 820 *band seismic stations*. Institut de Physique du Globe de Paris (IPGP). Retrieved 2019-  
 821 02-08, from <http://geoscope.ipgp.fr/networks/detail/G/> (Publisher: Institut  
 822 de Physique du Globe de Paris (IPGP)) doi: 10.18715/GEOSCOPE.G
- 823 Institute Of Geophysics Of The Academy Of Sciences Of The Czech Republic. (1973).  
 824 *Czech Regional Seismic Network*. Retrieved 2019-02-08, from [http://www.fdsn.org/](http://www.fdsn.org/doi/10.7914/SN/CZ)  
 825 [doi/10.7914/SN/CZ](http://www.fdsn.org/doi/10.7914/SN/CZ) (Publisher: International Federation of Digital Seismograph  
 826 Networks) doi: 10.7914/SN/CZ
- 827 Instituto Geografico Nacional, Spain. (1999). *Spanish Digital Seismic Network*. International  
 828 Federation of Digital Seismograph Networks. Retrieved 2020-08-21, from [http://](http://www.fdsn.org/networks/detail/ES/)  
 829 [www.fdsn.org/networks/detail/ES/](http://www.fdsn.org/networks/detail/ES/) (Publisher: International Federation of Digital  
 830 Seismograph Networks) doi: 10.7914/SN/ES
- 831 Jolivet, L., Romagny, A., Gorini, C., Maillard, A., Thinon, I., Couëffé, R., ...  
 832 Séranne, M. (2020). Fast dismantling of a mountain belt by mantle flow: Late-  
 833 orogenic evolution of pyrenees and liguro-provençal rifting. *Tectonophysics*, 776,  
 834 228312. Retrieved from [https://www.sciencedirect.com/science/article/pii/](https://www.sciencedirect.com/science/article/pii/S0040195119304275)  
 835 [S0040195119304275](https://www.sciencedirect.com/science/article/pii/S0040195119304275) doi: <https://doi.org/10.1016/j.tecto.2019.228312>
- 836 Klingelhoefer, F., Olivet, J., Aslanian, D., Bache, F., Moulin, M., Matias, L., ... Gailler,  
 837 A. (2008). Preliminary results from the sardinia deep seismic cruise on the western  
 838 sardinia and gulf of lions conjugate margin pair. In *Egu meeting april 2008*.
- 839 KNMI. (1993). *Netherlands Seismic and Acoustic Network*. Retrieved 2019-02-08, from  
 840 <http://rdsa.knmi.nl/network/NL/> (Publisher: Royal Netherlands Meteorological  
 841 Institute (KNMI)) doi: 10.21944/e970fd34-23b9-3411-b366-e4f72877d2c5
- 842 Kopp, H., Lange, D., Thorwart, M., Paul, A., Dannowski, A., Petersen, F., ... Xia, Y.  
 843 (2018). Rv maria s. merian fahrtbericht / cruise report msm71 lobster: Ligurian ocean  
 844 bottom seismology and tectonics research, las palmas (spain) – heraklion (greece)

845 07.02.-27.02.2018..

846 Kvapil, J., Plomerová, J., Kampfová Exnerová, H., Babuška, V., Hetényi, G., & Group,  
847 A. W. (2021). Transversely isotropic lower crust of variscan central europe imaged  
848 by ambient noise tomography of the bohemian massif. *Solid Earth*, 12(5), 1051–  
849 1074. Retrieved from <https://se.copernicus.org/articles/12/1051/2021/> doi:  
850 10.5194/se-12-1051-2021

851 Leprêtre, A., Klingelhoefer, F., Graindorge, D., Schnurle, P., Beslier, M.-O., Yelles, K., ...  
852 Bracene, R. (2013). Multiphased tectonic evolution of the central algerian margin  
853 from combined wide-angle and reflection seismic data off tipaza, algeria. *Journal of*  
854 *Geophysical Research: Solid Earth*, 118(8), 3899–3916.

855 Levander, A., Schmandt, B., Miller, M. S., Liu, K., Karlstrom, K. E., Crow, R. S., ...  
856 Humphreys, E. D. (2011). Continuing colorado plateau uplift by delamination-  
857 style convective lithospheric downwelling. *Nature*, 472(7344), 461-465. Retrieved  
858 from [https://EconPapers.repec.org/RePEc:nat:nature:v:472:y:2011:i:7344:](https://EconPapers.repec.org/RePEc:nat:nature:v:472:y:2011:i:7344:d:10.1038_nature10001)  
859 [d:10.1038\\_nature10001](https://doi.org/10.1038_nature10001)

860 Levshin, A., Yanovskaya, T., Lander, A., Bukchin, B., Barmin, M., Its, E., & Ratnikova,  
861 L. (1989). *Seismic Surface Waves in a Laterally Inhomogeneous Earth* (V. E. Keilis-  
862 Borok, Ed.). Kluwer Publ, Dordrecht, pp 129–182.

863 Lobkis, O. I., & Weaver, R. L. (2001). On the emergence of the green's function in the  
864 correlations of a diffuse field. *The Journal of the Acoustical Society of America*, 110(6),  
865 3011-3017. Retrieved from <https://doi.org/10.1121/1.1417528> doi: 10.1121/  
866 1.1417528

867 Lu, Y., Stehly, L., Brossier, R., Paul, A., & AlpArray Working Group. (2020, 03). Imaging  
868 Alpine crust using ambient noise wave-equation tomography. *Geophysical Journal In-*  
869 *ternational*, 222(1), 69-85. Retrieved from <https://doi.org/10.1093/gji/ggaa145>  
870 doi: 10.1093/gji/ggaa145

871 Lu, Y., Stehly, L., Paul, A., & AlpArray Working Group. (2018, 05). High-resolution  
872 surface wave tomography of the European crust and uppermost mantle from ambient  
873 seismic noise. *Geophysical Journal International*, 214(2), 1136-1150. Retrieved from  
874 <https://doi.org/10.1093/gji/ggy188> doi: 10.1093/gji/ggy188

875 Malusà, M. G., Guillot, S., Zhao, L., Paul, A., Solarino, S., Dumont, T., ...  
876 Yuan, H. (2021). The deep structure of the alps based on the civalps seis-  
877 mic experiment: A synthesis. *Geochemistry, Geophysics, Geosystems*, 22(3),

878 e2020GC009466. Retrieved from [https://agupubs.onlinelibrary.wiley.com/](https://agupubs.onlinelibrary.wiley.com/doi/abs/10.1029/2020GC009466)  
 879 doi/abs/10.1029/2020GC009466 (e2020GC009466 2020GC009466) doi: [https://](https://doi.org/10.1029/2020GC009466)  
 880 doi.org/10.1029/2020GC009466

881 Mascle, J., & Rehault, J.-P. (1990, 01). A revised seismic stratigraphy of the tyrrhenian  
 882 sea: implications for the basin evolution. , 617-637.

883 McKenzie, D. (1978). Some remarks on the development of sedimentary basins. *Earth and*  
 884 *Planetary science letters*, 40(1), 25–32.

885 Moschetti, M. P., Ritzwoller, M. H., Lin, F., & Yang, Y. (2010). Seismic evidence  
 886 for widespread western-us deep-crustal deformation caused by extension. *Nature*,  
 887 464(7290), 885-889. Retrieved from [https://EconPapers.repec.org/RePEc:nat:](https://EconPapers.repec.org/RePEc:nat:nature:v:464:y:2010:i:7290:d:10.1038_nature08951)  
 888 [nature:v:464:y:2010:i:7290:d:10.1038\\_nature08951](https://EconPapers.repec.org/RePEc:nature:v:464:y:2010:i:7290:d:10.1038_nature08951)

889 Nouibat, A., Stehly, L., Paul, A., Schwartz, S., Bodin, T., Dumont, T., ... AlpArray Work-  
 890 ing Group (2022, 12). Lithospheric transdimensional ambient-noise tomography of W-  
 891 Europe: implications for crustal-scale geometry of the W-Alps. *Geophysical Journal*  
 892 *International*. Retrieved from <https://doi.org/10.1093/gji/ggab520> (ggab520)  
 893 doi: 10.1093/gji/ggab520

894 Pascal, G., Mauffret, A., & Patriat, P. (1993). The ocean-continent boundary in the gulf  
 895 of lion from analysis of expanding spread profiles and gravity modelling. *Geophysical*  
 896 *Journal International*, 113(3), 701–726.

897 Peterson, J. R. (1993). *Observations and modeling of seismic background noise* (Tech. Rep.).  
 898 US Geological Survey.

899 Réhault, J.-P., Boillot, G., & Mauffret, A. (1984). The western mediterranean basin  
 900 geological evolution. *Marine Geology*, 55(3), 447-477. Retrieved from [https://](https://www.sciencedirect.com/science/article/pii/0025322784900811)  
 901 [www.sciencedirect.com/science/article/pii/0025322784900811](https://www.sciencedirect.com/science/article/pii/0025322784900811) (Geological  
 902 and Geodynamical Aspects on the Mediterranean) doi: [https://doi.org/10.1016/](https://doi.org/10.1016/0025-3227(84)90081-1)  
 903 [0025-3227\(84\)90081-1](https://doi.org/10.1016/0025-3227(84)90081-1)

904 Réhault, J.-P., Honthaas, C., Guennoc, P., Bellon, H., Ruffet, G., Cotten, J., ... Maury,  
 905 R. (2012). Offshore oligo-miocene volcanic fields within the corsica-liguria basin:  
 906 Magmatic diversity and slab evolution in the western mediterranean sea. *Journal of*  
 907 *Geodynamics*, 58, 73–95.

908 RESIF. (1995). *RESIF-RLBP French Broad-band network, RESIF-RAP strong motion*  
 909 *network and other seismic stations in metropolitan France*. Retrieved 2019-02-08,  
 910 from <http://seismology.resif.fr/#NetworkConsultPlace:FR> (Publisher: RESIF)

- 911 - Réseau Sismologique et géodésique Français) doi: 10.15778/resif.fr
- 912 Reynard, B. (2013). Serpentine in active subduction zones. *Lithos*, *178*, 171–185.
- 913 Rollet, N., Déverchère, J., Beslier, M.-O., Guennoc, P., Réhault, J.-P., Sosson, M.,  
914 & Truffert, C. (2002). Back arc extension, tectonic inheritance, and vol-  
915 canism in the ligurian sea, western mediterranean. *Tectonics*, *21*(3), 6-1-  
916 6-23. Retrieved from [https://agupubs.onlinelibrary.wiley.com/doi/abs/10](https://agupubs.onlinelibrary.wiley.com/doi/abs/10.1029/2001TC900027)  
917 [.1029/2001TC900027](https://agupubs.onlinelibrary.wiley.com/doi/abs/10.1029/2001TC900027) doi: <https://doi.org/10.1029/2001TC900027>
- 918 Roux, P., Sabra, K. G., Gerstoft, P., Kuperman, W., & Fehler, M. C. (2005). P-waves from  
919 cross-correlation of seismic noise. *Geophysical Research Letters*, *32*(19).
- 920 Royal Observatory Of Belgium. (1985). *Belgian Seismic Network*. Retrieved 2019-02-08,  
921 from <http://www.fdsn.org/doi/10.7914/SN/BE> (Publisher: International Federa-  
922 tion of Digital Seismograph Networks) doi: 10.7914/SN/BE
- 923 Sadeghi-Bagherabadi, A., Vuan, A., Aoudia, A., Parolai, S., T. A., Group, A.-S.-D. W., ...  
924 Tilmann, F. (2021). High-resolution crustal s-wave velocity model and moho geometry  
925 beneath the southeastern alps: New insights from the swath-d experiment. *Frontiers*  
926 *in Earth Science*, *9*, 188. Retrieved from [https://www.frontiersin.org/article/](https://www.frontiersin.org/article/10.3389/feart.2021.641113)  
927 [10.3389/feart.2021.641113](https://www.frontiersin.org/article/10.3389/feart.2021.641113) doi: 10.3389/feart.2021.641113
- 928 Sandwell, D. T., & Smith, W. H. (1997). Marine gravity anomaly from geosat and ers 1  
929 satellite altimetry. *Journal of Geophysical Research: Solid Earth*, *102*(B5), 10039–  
930 10054.
- 931 Sandwell, D. T., Yale, M., & Smith, W. (1995). Gravity anomaly profiles from ers-1, topex  
932 and geosat altimetry. *Eos Trans. AGU*, *76*(17), S89.
- 933 Schippkus, S., Zigone, D., Bokelmann, G., & the AlpArray Working Group. (2018, 06).  
934 Ambient-noise tomography of the wider Vienna Basin region. *Geophysical Journal In-*  
935 *ternational*, *215*(1), 102-117. Retrieved from <https://doi.org/10.1093/gji/ggy259>  
936 doi: 10.1093/gji/ggy259
- 937 Séranne, M. (1999). The gulf of lion continental margin (nw mediterranean) revisited  
938 by ibs: an overview. *Geological Society, London, Special Publications*, *156*(1), 15–  
939 36. Retrieved from <https://sp.lyellcollection.org/content/156/1/15> doi: 10  
940 [.1144/GSL.SP.1999.156.01.03](https://sp.lyellcollection.org/content/156/1/15)
- 941 Shapiro, N. M., & Singh, S. K. (1999, 08). A systematic error in estimating surface-wave  
942 group-velocity dispersion curves and a procedure for its correction. *Bulletin of the*  
943 *Seismological Society of America*, *89*(4), 1138-1142.

- 944 Slovenian Environment Agency. (2001). Seismic Network of the Republic of Slovenia.  
 945 Retrieved 2020-08-21, from <http://www.fdsn.org/doi/10.7914/SN/SL> (Publisher:  
 946 International Federation of Digital Seismograph Networks) doi: 10.7914/SN/SL
- 947 Snieder, R. (2004). Extracting the green's function from the correlation of coda waves: A  
 948 derivation based on stationary phase. *Physical Review E*, *69*(4), 046610.
- 949 SNSN. (1904). *Swedish National Seismic Network*. Retrieved 2019-02-08, from [http://](http://www.snsn.se/network/)  
 950 [www.snsn.se/network/](http://www.snsn.se/network/) (Publisher: Uppsala University, Uppsala, Sweden) doi:  
 951 10.18159/SNSN
- 952 Soergel, D., Pedersen, H. A., Stehly, L., Margerin, L., Paul, A., & AlpArray Working Group.  
 953 (2020, 10). Coda-Q in the 2.5–20 s period band from seismic noise: application to the  
 954 greater Alpine area. *Geophysical Journal International*, *220*(1), 202-217. Retrieved  
 955 from <https://doi.org/10.1093/gji/ggz443> doi: 10.1093/gji/ggz443
- 956 Swiss Seismological Service (SED) At ETH Zurich. (1983). National Seismic Networks  
 957 of Switzerland. Retrieved 2020-08-20, from [http://networks.seismo.ethz.ch/](http://networks.seismo.ethz.ch/networks/ch/)  
 958 [networks/ch/](http://networks.seismo.ethz.ch/networks/ch/) (Publisher: ETH Zürich) doi: 10.12686/SED/NETWORKS/CH
- 959 Takeo, A., Kawakatsu, H., Isse, T., Nishida, K., Sugioka, H., Ito, A., ... Suetsugu, D.  
 960 (2016). Seismic azimuthal anisotropy in the oceanic lithosphere and asthenosphere  
 961 from broadband surface wave analysis of obs array records at 60 ma seafloor. *Journal*  
 962 *of Geophysical Research: Solid Earth*, *121*(3), 1927–1947.
- 963 University Of Zagreb. (2001). *Croatian Seismograph Network*. Retrieved 2020-08-20, from  
 964 <http://www.fdsn.org/networks/detail/CR/> (Publisher: International Federation  
 965 of Digital Seismograph Networks) doi: 10.7914/SN/CR
- 966 van Hinsbergen, D. J., Torsvik, T. H., Schmid, S. M., Mañenco, L. C., Maffione, M., Vissers,  
 967 R. L., ... Spakman, W. (2020). Orogenic architecture of the mediterranean region  
 968 and kinematic reconstruction of its tectonic evolution since the triassic. *Gondwana*  
 969 *Research*, *81*, 79-229. Retrieved from [https://www.sciencedirect.com/science/](https://www.sciencedirect.com/science/article/pii/S1342937X19302230)  
 970 [article/pii/S1342937X19302230](https://www.sciencedirect.com/science/article/pii/S1342937X19302230) doi: <https://doi.org/10.1016/j.jgr.2019.07.009>
- 971 Wapenaar, K. (2004, Dec). Retrieving the elastodynamic green's function of an arbitrary  
 972 inhomogeneous medium by cross correlation. *Phys. Rev. Lett.*, *93*, 254301. Retrieved  
 973 from <https://link.aps.org/doi/10.1103/PhysRevLett.93.254301> doi: 10.1103/  
 974 PhysRevLett.93.254301
- 975 Weaver, R. L. (2005). Information from seismic noise. *Science*, *307*, 1568 - 1569.

- 976 Wolf, F. N., Lange, D., Dannowski, A., Thorwart, M., Crawford, W., Wiesenberg, L., ...  
 977 the AlpArray Working Group (2021). 3D crustal structure of the Ligurian Basin  
 978 revealed by surface wave tomography using ocean bottom seismometer data. *Solid*  
 979 *Earth*, 12(11), 2597–2613. Retrieved from [https://se.copernicus.org/articles/](https://se.copernicus.org/articles/12/2597/2021/)  
 980 [12/2597/2021/](https://se.copernicus.org/articles/12/2597/2021/) doi: 10.5194/se-12-2597-2021
- 981 Yan, F., Han, D.-h., Yao, Q., & Chen, X.-L. (2016, 05). Seismic velocities of halite salt:  
 982 Anisotropy, heterogeneity, dispersion, temperature, and pressure effects. *Geophysics*,  
 983 81(4), D293-D301. Retrieved from <https://doi.org/10.1190/geo2015-0476.1> doi:  
 984 10.1190/geo2015-0476.1
- 985 ZAMG-Zentralanstalt Für Meteorologie Und Geodynamik. (1987). Austrian Seismic Net-  
 986 work. Retrieved 2020-08-20, from <http://www.fdsn.org/doi/10.7914/SN/OE> (Pub-  
 987 lisher: International Federation of Digital Seismograph Networks) doi: 10.7914/SN/  
 988 OE
- 989 Zhao, L., Malusà, M. G., Yuan, H., Paul, A., Guillot, S., Lu, Y., ... Bodin, T. (2020, May).  
 990 Evidence for a serpentized plate interface favouring continental subduction. *Nature*  
 991 *Communications*, 11, 2171. Retrieved from [https://hal.archives-ouvertes.fr/](https://hal.archives-ouvertes.fr/hal-02560510)  
 992 [hal-02560510](https://hal.archives-ouvertes.fr/hal-02560510) doi: 10.1038/s41467-020-15904-7
- 993 Zhao, L., Paul, A., Solarino, S., & RESIF. (2018). *Seismic network XT: CIFALPS temporary*  
 994 *experiment (China-Italy-France Alps seismic transect)*. RESIF - Réseau Sismologique  
 995 et géodésique Français. doi: 10.15778/RESIF.XT2018

## 996 Supporting information

997 Additional Figures and information are presented as the Supplementary Material. Text S1  
 998 provides details on the processing applied to remove glitches of instrumental origin from ver-  
 999 tical and pressure component records of seven AlpArray seismic network broadband ocean-  
 1000 bottom seismometers (AASN BBOBSs). Text S2 describes how coherent signals are detected  
 1001 and used to reduce tilt- and compliance-induced noises in vertical-component records of the  
 1002 23 AASN OBSs used in this work. Table S1 and Figures S1 to S8 complement sections 2 to  
 1003 4 of the main text.